Mon. Not. R. Astron. Soc. **367,** 46–78 (2006) doi:10.1111/j.1365-2966.2005.09977.x

Late-type galaxies observed with SAURON: two-dimensional stellar and emission-line kinematics of 18 spirals

Katia Ganda,[1⋆] Jesús Falcón-Barroso,[2] Reynier F. Peletier,[1] Michele Cappellari,[2] Eric Emsellem,[3] Richard M. McDermid,[2] P. Tim de Zeeuw[2] and C. Marcella Carollo[4]

[1]*Kapteyn Astronomical Institute, Postbus 800, 9700 AV Groningen, the Netherlands*
[2]*Leiden Observatory, Postbus 9513, 2300 RA Leiden, the Netherlands*
[3]*Centre de Recherche Astrophysique de Lyon – Observatoire, 9 Avenue Charles André, 69230 Saint Genis Laval, France*
[4]*Eidgenössische Technische Hochschule Zurich, Hönggerberg HPF G4.3, CH-8092 Zurich, Switzerland*

Accepted 2005 December 2. Received 2005 November 21; in original form 2005 October 4

ABSTRACT

We present the stellar and gas kinematics of a sample of 18 nearby late-type spiral galaxies (Hubble types ranging from Sb to Sd), observed with the integral-field spectrograph SAURON at the 4.2-m William Herschel Telescope. SAURON covers the spectral range 4800–5380 Å, allowing us to measure the Hβ, Fe, Mg*b* absorption features and the emission in the Hβ line and the [O III]$\lambda\lambda$4959, 5007 Å and [N I]$\lambda\lambda$5198, 5200 Å doublets over a 33 × 41-arcsec^2 field of view. The maps cover the nuclear region of these late-type galaxies and in all cases include the entire bulge. In many cases the stellar kinematics suggests the presence of a cold inner region, as visible from a central drop in the stellar velocity dispersion. The ionized gas is almost ubiquitous and behaves in a complicated fashion: the gas velocity fields often display more features than the stellar ones, including wiggles in the zero-velocity lines, irregular distributions, ring-like structures. The line ratio [O III]/Hβ often takes on low values over most of the field, probably indicating a wide-spread star formation.

Key words: galaxies: bulges – galaxies: evolution – galaxies: formation – galaxies: kinematics and dynamics – galaxies: spiral.

1 INTRODUCTION

From a theoretical point of view, we have a well-defined paradigm for the formation of disc galaxies within the cold dark matter hierarchical structure formation scenario (Fall & Efstathiou 1980; Silk 2003): discs quietly settle and cool inside dark matter haloes, while bulges form through mergers of multiple haloes. However, some of the observed properties of spiral galaxies suggest a larger complexity in their formation history. The presence of bulges is not ubiquitous and their nature can be ambiguous. Evidence has accumulated in the past years showing that many bulges have a disc-like, sometimes exponential radial fall-off of the stellar density (Andredakis & Sanders 1994; Andredakis, Peletier & Balcells 1995; de Jong 1995; Courteau, de Jong & Broeils 1996; Carollo & Stiavelli 1998; Seigar et al. 2002; MacArthur, Courteau & Holtzmann 2003). Numerical simulations seem to suggest that the dissolution of bars inside the discs may trigger the formation of three-dimensional stellar structures with roughly exponential profiles (Combes et al. 1990; Pfenniger & Norman 1990; Raha et al. 1991; Norman, Sellwood & Hasan 1996); this could mean that some bulges form through the evolution of dynamical instabilities in the disc. Quite recently, the quality of imaging data made available through *Hubble Space Telescope* (*HST*) boosted the study of the inner regions of spiral galaxies, showing that they can host a variety of structures: bulges, nuclear star clusters, stellar discs, small bars, double bars, star forming rings (Carollo et al. 1997; Carollo, Stiavelli & Mack 1998; Carollo 1999; Pérez-Ramírez et al. 2000; Böker et al. 2002; Carollo et al. 2002; Falcón-Barroso, Peletier & Balcells 2002; Laine et al. 2002; Allard, Peletier & Knapen 2005), without there being an agreement about their origin and evolutionary pattern. Ongoing large projects like the panchromatic Spitzer Infrared Nearby Galaxies Survey (SINGS) (Kennicutt et al. 2003) which makes use of observations at infrared, visible and UV wavelengths represent a very useful approach to building a comprehensive picture of galactic structure, but at the moment rely mostly on imaging. Looking at disc galaxies from a spectroscopic perspective would add kinematic information and insight into stellar populations which cannot come from imaging, and could help us tracing their star formation and mass assembly histories.

Contrary to the massive spheroids, the stellar populations and kinematics of late-type disc-dominated galaxies are poorly known, due to the difficulty of reliably measuring and interpreting such diagnostics in low surface brightness environments which are so full of dust, star formation and substructures, not much attention has been paid to the spectroscopic counterpart of all the mentioned imaging that has been carried out. There are a few exceptions to this

⋆E-mail: katia@astro.rug.nl

statement: Böker et al. (2001) started a project on Space Telescope Imaging Spectrograph (STIS) long-slit spectroscopy of 77 nearby late-type spiral galaxies previously imaged with *HST*/Wide Field Planetary Camera 2 (WFPC2); first results are discussed in Böker et al. (2003); Walcher et al. (2005) analysed UV slit-spectroscopy of the nuclei of nine late-type spirals; these studies are mainly focused on the nature of the innermost components, in particular on the nuclear star clusters.

We are currently engaged in a study aimed at investigating the properties of the nuclear regions of very late-type galaxies. In such environments, long-slit spectra are too limited to be useful for modelling and interpretation and have generally been used only to discuss the properties of emission lines (see e.g. Matthews & Gallagher 2002, who measure the position–velocity curve of 21 extreme late-type spiral galaxies using the Hα emission line). Here, we present deep integral-field spectroscopy that not only makes it easier to study the kinematics and physical properties of stars and gas, but also allows to study and model the stellar populations.

We were granted six nights at the William Herschel Telescope (WHT) of the Observatorio del Roque de los Muchachos in La Palma, Spain, to obtain two-dimensional spectroscopy with the integral-field Spectrographic Areal Unit for Research on Optical Nebulae (SAURON), which was custom built for a representative census of elliptical and lenticular galaxies, and Sa bulges (the so-called SAURON survey, see Bacon et al. 2001 and de Zeeuw et al. 2002, hereafter, respectively, Paper I and Paper II). The present work can be regarded as a natural extension of the SAURON survey towards the end of the Hubble sequence. Our purpose was to use SAURON in order to map the stellar and gaseous (Hβ, [O III], [N I]) kinematics and the absorption line-strength distributions of the indices Hβ, Mg, Fe, in the region 4800–5380 Å. In this paper, we present the observations and data reduction and the resulting kinematical maps for 18 Sb–Sd galaxies. The data and maps will be made available via the SAURON website (http://www.strw.leidenuniv.nl/sauron).

The paper is structured as follows. Section 2 describes the sample selection and characteristics. Section 3 summarizes the observations and data reduction. Section 4 describes the methods applied to calculate the stellar and gaseous kinematics from our spectra. Section 5 carries out a comparison with previous measurements. Section 6 presents and discuss the kinematical maps and looks in particular at the behaviour of the stellar velocity dispersion. Finally, Section 7 summarizes the results. Detailed modelling and interpretation of the data will come in future papers.

2 THE SAMPLE

Our sample galaxies were optically selected ($B_T < 12.5$, according to the values given in de Vaucouleurs et al. 1991, hereafter RC3) with *HST* imaging available from WFPC2 and/or Near Infrared Camera and Multi-Object Spectrometer (NICMOS). In practice, the galaxies were chosen from objects lists of recent imaging projects with *HST* (Carollo et al. 1997, 1998; Böker et al. 2002; Carollo et al. 2002; Laine et al. 2002). Their morphological type ranges between Sb and Sd, following the classification reported in NASA/IPAC Extragalactic Database (NED)[1] (from RC3). Galaxies in close interaction and Seyferts were discarded. Only galaxies with $0 <$ right ascension $< 15^{\rm h}$ and $\delta > -20^\circ$ were selected, to fulfil a visibility criterion during the allocated nights. The resulting sample contains 18 nearby galaxies.

In Table 1 we list properties already measured and available through public catalogues, while in Fig. 1 we represent graphically the range spanned by our sample galaxies in a number of global and nuclear properties. This can be useful for a visual comparison with the galaxies of the SAURON survey (see figs 1 and 3 of Paper II). Panel (a) shows the distribution of the selected galaxies in the plane M_B–ϵ_{25}. M_B is the absolute magnitude in the B band and ϵ_{25} is the ellipticity, derived from the axial ratio at the 25 mag arcsec^{-2} isophotal level in B. This panel shows that there is a lack of high-ellipticity objects, indicating that our disc galaxies are generally far from being edge-on systems. Panel (b) plots the effective $B - V$ colour versus the central velocity dispersion σ; a relatively tight trend is recognizable, since galaxies with higher velocity dispersions tend to be redder. Panel (c) plots the effective $B - V$ colour versus the morphological type; colours become bluer with later types. Panel (d) shows the distribution of our galaxies in the Tully–Fisher plane: M_B versus the inclination-corrected rotation velocity, obtained as $W_{20_c} = W_{20}/\sin(i)$, where W_{20} is the 21-cm line width at 20 per cent of the peak and i the inclination between line of sight and polar axis. The overplotted solid line is the Tully–Fisher relation, as determined by Verheijen (2001) for the B band from a sample of 45 galaxies with measured H I global profile: $M_B = -2.91$–$6.8\log(W_{20_c})$. In the figure, all the galaxies with inclination below 45° are marked with an asterisk, since the reported relation was established on the basis of higher-inclination objects, one can see that all the galaxies that deviate most from the red line have low inclination, although not all of the low-inclination galaxies are deviant. Panel (e) presents the relation between total luminosity (absolute blue magnitude M_B) and central velocity dispersion; the galaxies cover a range of ≈100 in luminosity and a factor of ≈5 in velocity dispersion and become more luminous with increasing velocity dispersion. To conclude, panel (f) plots M_B against the morphological type; the luminosity tends to decrease as the galaxies become later in type, as shown also by de Jong (1996). The quantities plotted in this figure are all derived from catalogues, mainly from RC3 and HyperLeda,[2] (for a description and a list of references, see caption to Table 1), except for the central velocity dispersion. Since previously existing central velocity dispersion values are available only for six of the galaxies in our sample, we decided to measure the central velocity dispersion from our own spectra. The measured spectra in a central aperture (2.4×2.4 arcsec^2) were combined to give an averaged spectrum from which we computed the stellar kinematics, using methods which we will present and discuss later in this paper. The resulting σ values are taken as central velocity dispersions, listed in Table 1 and used in Fig. 1. In Section 5, we will provide a qualitative comparison between our central velocity dispersions and the literature values, for the six galaxies for which we could find references.

3 OBSERVATIONS AND DATA REDUCTION

Observations of the 18 late-type galaxies were carried out in 2004 January 20–26, using the integral-field spectrograph SAURON attached to the 4.2-m WHT. For each of the 18 galaxies, Table 2 lists the number of 1800-s exposures that we took.

We used the low spatial resolution mode of SAURON, giving a field of view (FOV) of 33×41 arcsec^2. The spatial sampling of individual exposures is determined by an array of 0.94×0.94-arcsec^2 lenses. This produces 1431 spectra per pointing over the

[1] http://nedwww.ipac.caltech.edu

[2] http://leda.univ-lyon1.fr

Table 1. Properties of our 18 galaxies. (1) Galaxy identifier. (2) Hubble type (RC3 through NED). (3) Numerical morphological type (RC3). (4) Heliocentric neutral hydrogen velocity in km s^{-1} (RC3, via VizieR). (5) Absolute blue magnitude M_B in mag (quoted from HyperLeda), computed from the corrected apparent magnitude and the distance modulus (also listed in HyperLeda); a Virgocentric flow model with $v_{\rm virgo} = 208$ km s^{-1}, a Hubble constant $H_0 = 70$ km s^{-1} Mpc^{-1} and the correction to the Local Group centroid of Yahil, Tammann & Sandage (1977) are adopted. (6) Effective $(B-V)_{\rm e}$ colour in mag; values marked with 'L' have been taken from HyperLeda, the others from RC3. (7) Projected diameter at the isophotal level of 25 mag arcsec^{-2} in the B band, in arcsec (RC3). (8) Effective radius $R_{\rm e}$ in the B band, in arcsec (RC3). (9) Ellipticity ϵ_{25} of the contour of 25 mag arcsec^{-2} B surface brightness (RC3). (10) Disc inclination in degrees, calculated from the axis ratio listed in RC3. (11) PA of the major axis, in degrees (RC3); values marked with 'g' are taken from Grosbøl (1985). (12) Central velocity dispersion σ in km s^{-1}, from our own measurement (averaging the spectra in a central 2.4 × 2.4-arcsec^2 aperture and measuring the kinematics on the resulting spectrum, as explained in the text). (13) Width of the 21-cm neutral hydrogen line at 20 per cent of the peak in km s^{-1} (RC3), corrected for the disc inclination, as listed in column (10).

NGC (1)	Type (2)	T (3)	V_{21} (4)	M_B (5)	$(B-V)_{\rm e}$ (6)	d_{25} (7)	$R_{\rm e}$ (8)	ϵ_{25} (9)	i (10)	PA (11)	σ (12)	$W_{20\ c}$ (13)
488	SA(r)b	3.0	2269	−21.71	0.96	315	52	0.260	42	15	196	675
628	SA(s)c	5.0	656	−20.29	0.64	629	144	0.088	24	25	54	190
772	SA(s)b	3.0	2458	−22.23	0.86	435	77	0.411	54	130	120	583
864	SAB(rs)c	5.0	1560	−20.54	0.63	281	97	0.241	41	20	65	356
1042	SAB(rs)cd	6.0	1373	−19.83	0.62	281	95	0.224	39	43$^{\rm g}$	55	179
2805	SAB(rs)d	7.0	1734	−20.75	0.54	379	128	0.241	41	125	46	181
2964	SAB(r)bc	4.0	1321	−19.74	0.75	173	26	0.451	57	97	101	372
3346	SB(rs)cd	6.0	1260	−18.89		173		0.129	29	111$^{\rm g}$	48	338
3423	SA(s)cd	6.0	1011	−19.54		228	36	0.149	32	10	49	337
3949	SA(s)bc	4.0	798	−19.60	0.49$^{\rm L}$	173		0.425	55	120	61	338
4030	SA(s)bc	4.0	1460	−20.27	0.88$^{\rm L}$	250		0.276	44	27	100	503
4102	SAB(s)b?	3.0	837	−19.38	0.97$^{\rm L}$	181		0.425	55	38	150	385
4254	SA(s)c	5.0	2407	−22.63	0.65	322	56	0.129	29	62$^{\rm g}$	72	537
4487	SAB(rs)cd	6.0	1037	−19.12		250		0.324	47	75	51	297
4775	SA(s)d	7.0	1567	−19.81		128		0.067	21	52$^{\rm g}$	42	342
5585	SAB(s)d	7.0	305	−18.32	0.49	345	102	0.354	50	30	42	204
5668	SA(s)d	7.0	1583	−19.65	0.70	199	38	0.088	24	164$^{\rm g}$	53	280
5678	SAB(rs)b	3.0	1922	−21.30	0.88$^{\rm L}$	199		0.510	61	5	103	452

SAURON FOV; another 146 lenses sample a region 1.9 arcmin away from the main field in order to measure simultaneously the sky background. SAURON delivers a spectral resolution of 4.2 Å full width at half-maximum (FWHM) and covers the narrow spectral range 4800–5380 Å (1.1 Å pixel^{-1}). This wavelength range includes a number of important stellar absorption lines (e.g. Hβ, Fe, Mgb) and potential emission lines as well (Hβ, [O III], [N I]). For a more exhaustive description of the instrument, see Paper I and in particular Table 1 there.

For each galaxy, two to six largely overlapping exposures of 1800 s were typically obtained (Table 2). An offset of a few arcseconds, which corresponds to a few spatial elements, was introduced between consecutive exposures to avoid systematic errors due, for example, to bad CCD regions. Fig. 2 outlines the (approximate) position of the SAURON pointings overlaid on R-band Digital Sky Survey images of our galaxies, showing that our observations cover the nuclear regions.

3.1 Data reduction

We reduced the SAURON observations using the dedicated software XSAURON developed at the Centre de Recherche Astronomique de Lyon (CRAL; Paper I). During the observing run, arc exposures were taken before and after each galaxy exposure for wavelength calibration purposes. Tungsten lamp exposures were also taken every night in order to build the extraction mask. At the telescope, we had a misalignment of ≈1° between the columns of the CCD and the dispersion direction. To correct for this misalignment and avoid interference patterns due to uneven sampling of the data, we decided to rectify the spectra by rotating all of the frames by the same amount (≈1°) and in the opposite sense to the mentioned misalignment, at a very early stage of the reduction, by means of the IRAF[3] tasks geomap and geotran, available from the IMAGES.IMMATCH package. The reduction steps include thus bias and dark subtraction, rotation of all the frames, extraction of the spectra using the fitted mask model, wavelength calibration, low-frequency flat-fielding, cosmic ray removal, homogenization of the spectral resolution over the FOV, sky subtraction and flux calibration of the spectra, although the data were not necessarily collected under photometric conditions. The individually extracted and calibrated data cubes were finally merged by truncating the wavelength domain to a common range, recentring the exposures using reconstructed images and combining the spectra, while correcting also for the effect of atmospheric refraction. In this process, the data cubes were spatially resampled to a common grid, so that the final merged data cube is sampled on to a rectangular grid with 0.8 × 0.8-arcsec^2 pixels. The improvement in spatial sampling with respect to the individual data cubes is due to the dithering of exposures.

4 ANALYSIS AND METHODS

In order to ensure the measurement of reliable stellar kinematics, we spatially binned our merged data cubes using the Voronoi two-dimensional binning algorithm of Cappellari & Copin (2003), creating compact bins with a minimum signal-to-noise ratio $({\rm S/N})_\star \approx$

[3] IRAF is distributed by the National Optical Astronomy Observatories, which are operated by the Association of Universities for Research in Astronomy, Inc., under cooperative agreement with the National Science Foundation.

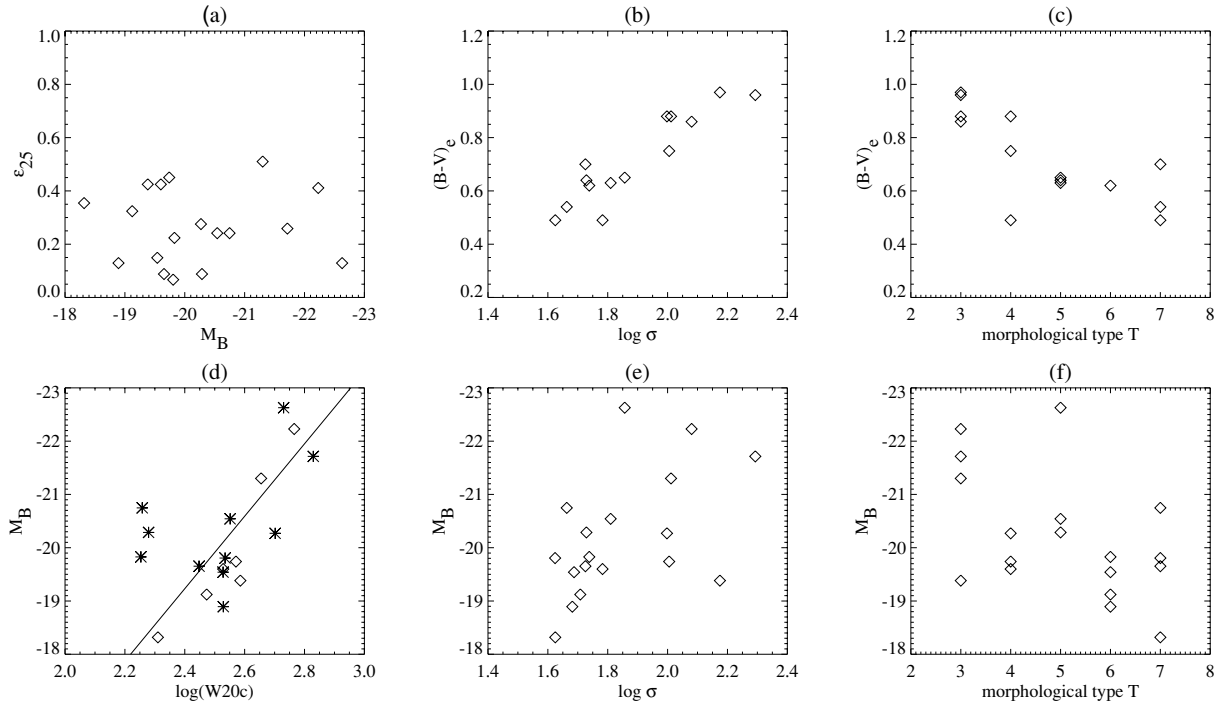

Figure 1. (a) Distribution of the 18 spiral galaxies in the plane ellipticity ϵ_{25} – absolute blue magnitude M_B; (b) effective $B-V$ colour versus central velocity dispersion σ (in logarithmic units; we note here once and for all that throughout the paper we will refer to decimal logarithms simply as logarithms); (c) effective $B-V$ colour versus morphological type; (d) absolute magnitude M_B versus the inclination-corrected rotation velocity (in logarithmic units); the overplotted solid line indicates the standard Tully–Fisher relation (see the text for further details); (e) M_B plotted versus central velocity dispersion σ (in logarithmic units); (f) M_B versus morphological type. The numerical values for the plotted quantities are derived from public catalogues (see Table 1), except the values for σ, that come from our own measurements, as explained in the text.

Table 2. Number of exposures of 1800 s each per galaxy.

NGC	#	NGC	#
488	3	3949	3
628	1+4[a]	4030	5
772	5	4102	5
864	4	4254	2
1042	4	4487	4
2805	6	4775	4
2964	2	5585	5
3346	6	5668	5
3423	6	5678	4

[a] For the first exposure of NGC 628 we pointed the telescope on a star offset by ≈13 arcsec with respect to the galaxy centre; so we have 2 slightly different pointings on this galaxy.

60 per resolution element. However, most of the spectra in the central regions have a $(S/N)_\star$ greater than 60, so a large fraction of the original spatial elements remains unbinned.

4.1 Stellar kinematics

We measured the stellar kinematics on each spectrum in our binned data cubes using the penalized pixel fitting (pPXF) method by Cappellari & Emsellem (2004). A linear combination of template stellar spectra, convolved with a line-of-sight velocity distribution described as a Gauss–Hermite expansion (Gerhard 1993; van der Marel & Franx 1993), is fitted to each galaxy spectrum by χ^2 minimization in pixel space, using a penalty term to suppress noise. While fitting, the spectral regions that are potentially affected by nebular emission (corresponding to the Hβ, [O III], [N I] lines) are masked out. A low-order polynomial (generally of order 6) is also included in the fit to account for small differences in the flux calibration between the galaxy and the template spectra. This allows us to derive the mean velocity (V), velocity dispersion (σ) and the higher-order Gauss–Hermite moments (h_3 and h_4). As stellar templates we used a library of single-age, single-metallicity population models from Vazdekis (1999), from which we selected 39 models characterized by $1.00 \leqslant \mathrm{Age} \leqslant 17.78$ Gyr, $-1.68 \leqslant [\mathrm{Fe/H}] \leqslant +0.20$. This is similar to what has been done by Falcón-Barroso et al. (2006, hereafter Paper VII) for the analysis of the 24 Sa galaxies part of the SAURON survey.

As we will show in Section 6, our galaxies display stellar velocity dispersions often lower than those measured in the early-type galaxies of the SAURON survey (Emsellem et al. 2004, hereafter Paper III). SAURON has an instrumental dispersion of 108 km s^{-1}, while our measured velocity dispersions are in many cases below that level (see the central values for σ listed in Table 1). Thus, one might be concerned that velocity dispersions significantly below the instrumental dispersion cannot be reliably measured. This issue has already been addressed in Paper III: it reports tests of the uncertainties on the measured σ via Monte Carlo simulations which prove that for a spectrum with $(S/N)_\star \approx 60$ and $\sigma \approx 50$ km s^{-1}, the pPXF method will output velocity dispersions differing from the intrinsic one by no more than 10 km s^{-1}, a value within the measured error.

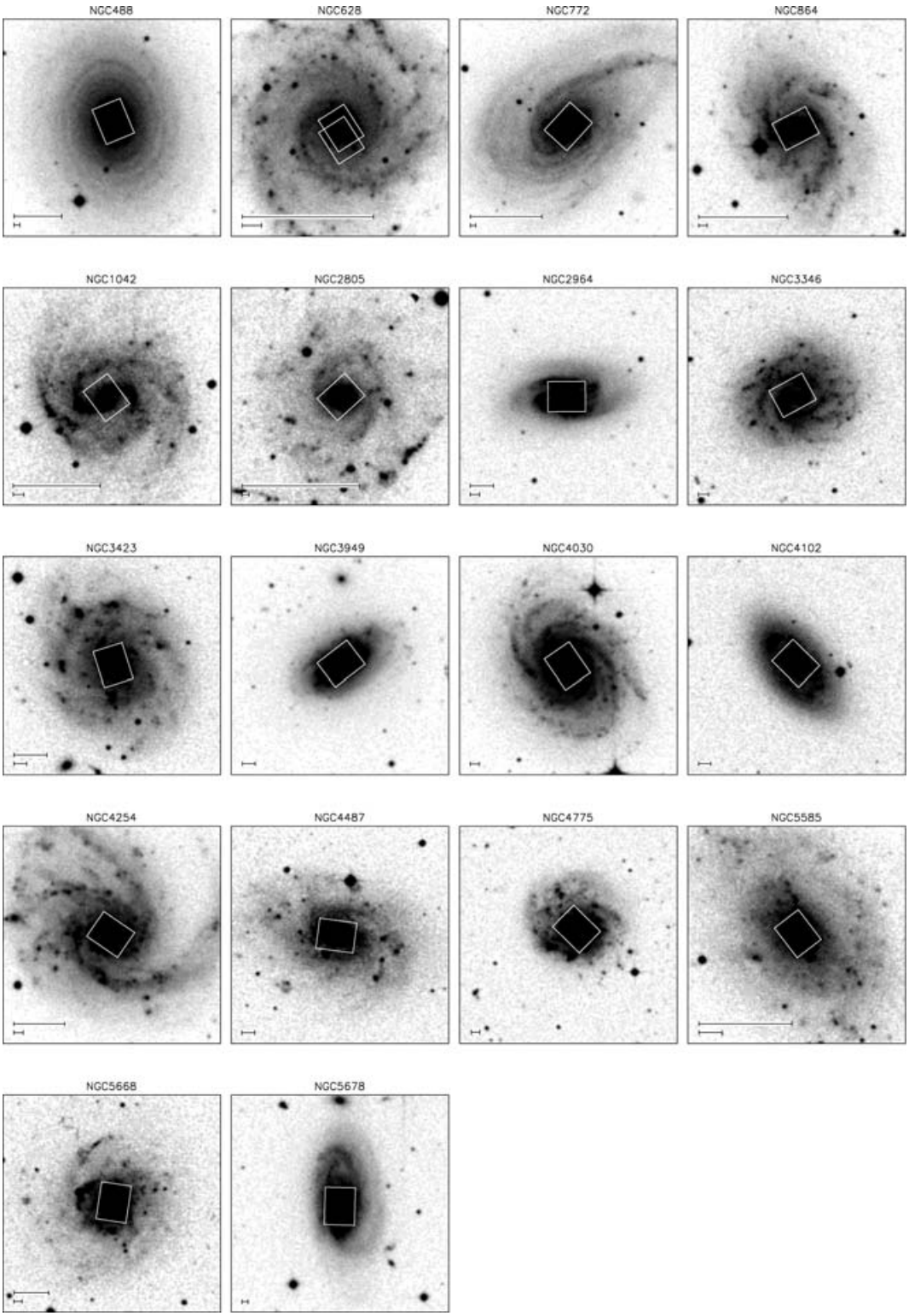

Figure 2. *R*-band Digital Sky Survey images of all 18 late-type spirals in the sample. The size of each image is $4 \times 4\,\mathrm{arcmin}^2$ and the orientation is such that north is upwards and east is towards left-hand side. Overplotted on each image are the positions of the SAURON pointings. The small bar at the bottom left-hand corner of each image corresponds to the linear length of 1 kpc; when the effective radius is available from RC3 (Table 1), another bar indicating the size of $1R_\mathrm{e}$ is provided, above the 1-kpc bar.

Another technical issue related to the low velocity-dispersion values is that when the observed velocity dispersion is less than about 2 pixels ($\sigma \leqslant 120\,\mathrm{km\,s^{-1}}$), it becomes more difficult to measure the Gauss–Hermite moments h_3 and h_4 at our minimum $(\mathrm{S/N})_\star \approx 60$; in those cases the penalization in pPXF then biases the solutions towards a Gaussian (Cappellari & Emsellem 2004). In practice, one expects the measured higher moments to be significant only in the galactic regions where the velocity dispersion or $(\mathrm{S/N})_\star$ are high.

4.2 Gas kinematics

Nebular emission is almost ubiquitous in our sample of 18 spiral galaxies. Thus, we have decided to apply a 'double-binning scheme', in order to compute the gas kinematics on bins smaller than the ones with $(S/N)_\star = 60$ on which we calculated the stellar kinematics as described above. The large amount of gas in fact allows us to reliably measure the kinematics of emission lines at a lower S/N level, and having smaller bins prevents loss of spatial resolution, especially in the outer regions. To do this, we proceed as follows.

We call 'star bins' the previously introduced Voronoi bins with minimum $(S/N)_\star = 60$. We first reconstruct the gas map by running pPXF on each single unbinned spectrum (single-lens spectrum) keeping fixed the stellar kinematics at the values determined for the star bin to which the spectrum belongs, thus fitting only for the stellar template and polynomial coefficients; this is done again by masking out the spectral regions potentially affected by emission. We recover the gas spectrum by subtracting the best fit from the original spectrum. For each gas spectrum we compute the $(S/N)_{gas}$ of the [O III] line taking the peak of the considered gas spectrum over the [O III] region and dividing by the noise, calculated on the gas spectrum over the emission-free part of the SAURON range. For the $(S/N)_{gas}$ determination, we could have used one of the other emission lines in the SAURON spectral range, e.g. Hβ or [N I], but they both present disadvantages compared to [O III]. In fact, the lines of the [N I] doublet are normally quite weak, and it is difficult to measure their kinematics and amplitude; the Hβ emission can instead be contaminated by stellar absorption at the same wavelength. At this stage, we bin the merged data cube to a minimum $(S/N)_{gas}$ of 5, according to the $(S/N)_{gas}$ values found for each single gas spectrum. We end up with a 'gas-binned' data cube. We call these bins 'gas bins'.

In a second step, we determine the gas kinematics for each gas bin. We proceed by running pPXF on the average of all the star-binned spectra that have some spatial intersection with the considered gas bin. This is the input stellar kinematics for our determination of the gas kinematics.

The actual computation of the gas kinematics parameters requires a careful separation of the line emission from the stellar absorption. We follow the procedure described in Sarzi et al. (2006; hereafter Paper V) and in Paper VII that has been fully tested on the SAURON survey galaxies. For each gas-binned spectrum, the method relies on an iterative search for the emission-line velocities and velocity dispersions, while linearly solving at each step for the line amplitudes and the optimal combination of the stellar templates. The fit is performed over each 'gas-binned' spectrum, and no masking is applied, in contrast to the stellar kinematics determination. A multiplicative Legendre polynomial of order 6 is included in the fit to correct for small differences in the flux calibration between the galaxy spectrum and the library of models.

Most of our galaxies have conspicuous gas emission, so we proceed by fitting the Hβ and [O III] lines independently, in order to detect differences in the kinematics of the two lines, if present. The [N I] lines are instead forced to share the same kinematics with Hβ (see Paper V and Paper VII for details on the method).

We have visually inspected the emission-line profiles in our data cubes in order to assess the applicability of our fitting method, which fits a single Gaussian profile to each line in the SAURON wavelength range. In the large majority of cases, we did not find deviations from pure Gaussians. Only NGC 2964 and 4102 present complex line profiles, but limited to specific regions possibly related to activity (see the description of individual objects in Section 6.4). This lack of complex line profiles may well be caused by the limited instrumental spectral resolution. For completeness, in Fig. 3 we show for NGC 4102 a spectrum where the [O III]5007 Å line does not resemble a single Gaussian and a spectrum where the line profiles instead do not differ from the Gaussian fit; there we present also the [O III] flux and velocity maps, in order to spatially locate the mentioned spectra.

5 COMPARISON WITH PUBLISHED MEASUREMENTS

The methods described in the previous sections were used to measure the stellar and gaseous kinematics and the amount of gas emission for the 72 galaxies of the SAURON survey (Paper III, Paper V and Paper VII). The quoted papers showed that the methods give results in agreement with previous measurements.

We also carried out a direct comparison with previous work. As already mentioned in Section 2, measurements of the stellar velocity dispersion are available for one-third of our sample. In addition, those few references are very heterogeneous and in some cases do not give all the information required to perform a careful and systematic comparison. In any case, we can qualitatively investigate the agreement of the central aperture velocity dispersion listed in Table 1 with the literature. The left-hand panel of Fig. 4 plots our measurements against the average of the existing values[4] (if more than one). Overplotted with a dotted line is the 1:1 relation. Uncertainties in the literature values are taken from the references; as for our own measurements, we give an estimate of the errors by running pPXF on the single-lens spectra within our aperture and looking at the scatter in the resulting velocity dispersions. The agreement is generally satisfactory; the only deviant galaxy is NGC 4254, for which the only references we could find date back from the 1980s (Whitmore, Kirshner & Schechter 1979; Tonry & Davies 1981).

In the case of the gas measurements, as a source for our literature comparison we choose the Palomar spectroscopic survey of Ho, Filippenko & Sargent (1995, 1997), which includes 11 out of our 18 galaxies. We compare the [O III]/Hβ line ratio and the width of the forbidden emission, represented by the [O III] and [N II]6583 Å lines of the SAURON and Palomar samples, respectively. To perform a proper comparison, we measured the [O III]/Hβ line ratio and [O III] FWHM on central spectra obtained extracting from our data cubes a central aperture that matches the size (2×4 arcsec^2) and orientation of the Palomar long-slit observations. Uncertainties in the [N II] FWHM in the Palomar survey are typically $\approx$10 per cent, except for NGC 3346 and 3949, where Ho et al. (1997) report only the 3σ upper limit; for the [O III]/Hβ line ratio, the quoted uncertainties are around 30–40 per cent, except the case of NGC 488, where the uncertainty is $\approx$50 per cent. For our SAURON data, errors on the [O III] line width come from the fitting procedure and vary in percentage from galaxy to galaxy, while an upper limit on the uncertainties on the [O III]/Hβ line ratio comes from the typical errors on the line fluxes estimate given in Paper V.

The central panel of Fig. 4 plots the SAURON against Palomar [O III]/Hβ line ratio. The agreement appears to be reasonable, with all the galaxies lying on the 1:1 relation (indicated by the dotted line in Fig. 4) within the error bar, with the exception of NGC 3949. The right-hand panel compares the FWHMs of the forbidden lines, and the agreement appears to be less satisfactory. In particular,

[4] From Shapiro, Gerssen & van der Marel (2003) for NGC 4030 and from HyperLeda for NGC 488, 628, 772, 2964 and 4254.

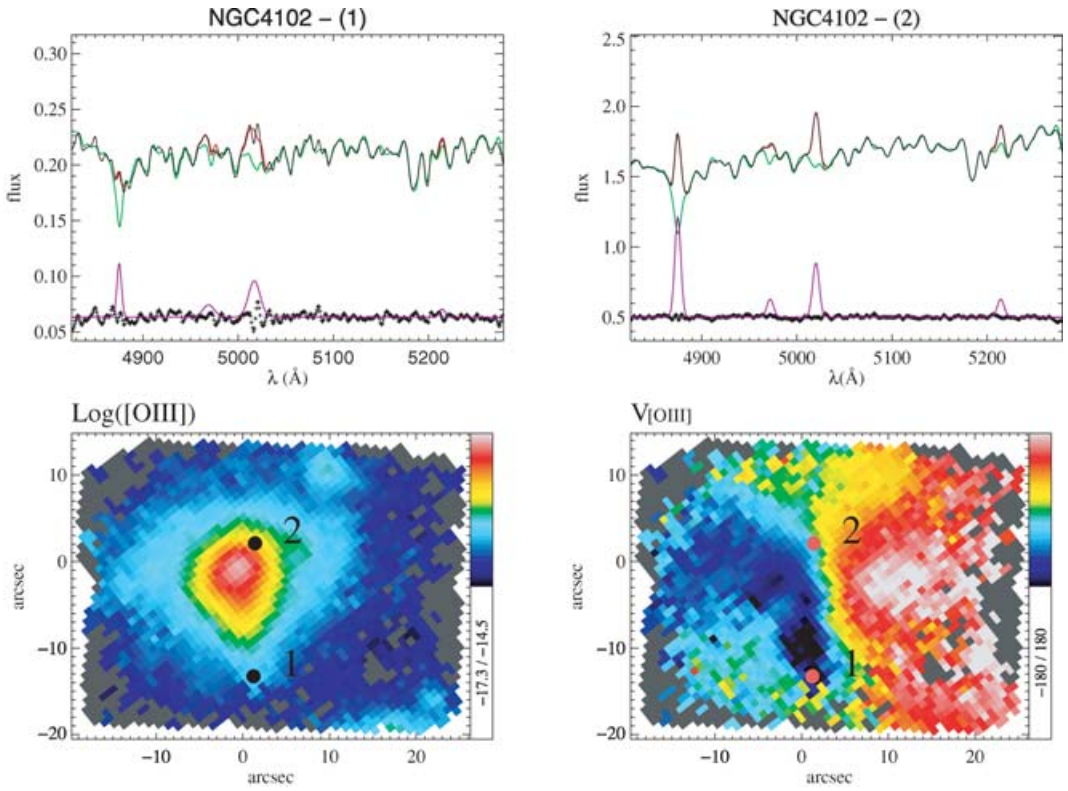

Figure 3. In the top left-hand panel we show for NGC 4102 a spectrum where the [O III] lines are only badly fitted by a single Gaussian; in the plot, the black solid line represents the galaxy spectrum; the red line is the full spectrum fit; the green solid line is the best-fitting combination of stellar templates, convolved with the kinematics; at the bottom of the panel, the purple line is the pure-emission spectrum and the black dotted line represents the residuals from the fit; a constant has been added to both. Along the vertical axis, the flux is in units of 10^{-16} erg cm^{-2} s^{-1}. The top right-hand panel shows a spectrum for the same galaxy where there are no deviations from Gaussianity in the line profiles. This is an example of the typical behaviour of our spectra and also illustrates the quality of fit that we obtain. In the second row, the [O III] flux (in erg cm^{-2} s^{-1} and logarithmic scale) and velocity (in km s^{-1}) maps are shown (bottom left- and right-hand panels, respectively); the location of the two representative spectra is marked on the maps with a dot. For a description of the maps, we refer the reader to Section 6.1.

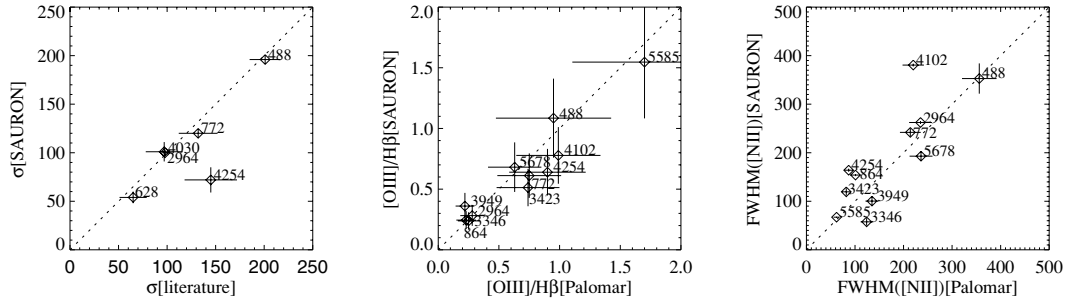

Figure 4. Literature comparison for stars (left-hand panel) and gas measurements (central and right-hand panels). Left-hand panel: SAURON against literature central stellar velocity dispersion (in km s^{-1}); central panel: SAURON against Palomar [O III]/Hβ line ratio; right-hand panel: SAURON against Palomar forbidden line width (in km s^{-1}). In each of the plots, the dotted line marks the 1:1 relation and the NGC galaxy identifiers are indicated close to the corresponding symbol; see the text for further details.

NGC 4102 lies well above the 1 : 1 relation; this is due to the broadening of the [O III] lines in this galaxy, where the single Gaussian used in our method fails to reproduce the line profile, as demonstrated at the end of the previous section. We stress the fact that the Palomar slit was oriented in the direction of the galactic region where the lines are double peaked (see Sections 4.2 and 6.4.12); our extracted aperture tests then that region and thus it is not a surprise that the comparison is not very accurate. In fact, a tight correlation between the widths of the [O III] and [N II] lines is expected if the lines are produced in low-density regions (Ho et al. 1997), and it is not clear that this condition is satisfied in all objects.

6 OBSERVED STELLAR AND GAS KINEMATICS

This section presents our results for the 18 spiral galaxies and points out and briefly describes some interesting features detectable in the maps. We first show the maps (Section 6.1), then discuss some

properties of the stellar and gaseous kinematics of the sample as a whole (Sections 6.2 and 6.3), and in the end give a detailed description of the individual galaxies (Section 6.4).

6.1 Stellar and gas flux and kinematics: the maps

Figs 5(a)–(r) present the flux and kinematical maps of stars and gas for our sample of 18 spiral galaxies, obtained as explained in Sections 4.1 and 4.2. For each object, in the first row we give the unsharp-masked optical image of the galaxy from *HST*[5] together with the UGC number when available, the FK5 2000 coordinates, the absolute blue magnitude, the ellipticity and the morphological type; NGC 772 represents an exception in that respect, since an optical space-based image is not available: we therefore show the unsharp-masked SAURON image instead; the second row contains the total intensity reconstructed by collapsing the SAURON spectra in the wavelength direction (in mag arcsec^{-2}, with an arbitrary zero-point), and the stellar velocity and velocity dispersion (in km s^{-1}); the third and fourth rows contain, respectively, the Hβ and [O III] flux (in erg cm^{-2} s^{-1} and logarithmic scale) and kinematics (velocity and velocity dispersion, in km s^{-1}); finally, the fifth row presents the line ratio [O III]/Hβ, in logarithmic scale, and the stellar h_3 and h_4 kinematical moments. Overplotted on each map are the isophotal contours. All the plotted velocities are systemic velocity subtracted; the same systemic velocity is assumed for stars and gas. No inclination correction to the kinematics has been applied, thus the plotted velocities are in all cases projected velocities. The stellar kinematics is shown on the $(S/N)_\star = 60$ star bins, while the gas parameters are plotted on the $(S/N)_{gas} = 5$ gas bins. In each figure, the arrow and its associated dash at the top of the page, close to the galaxy name, indicate the orientation of the maps, pointing to the north and east directions, respectively.

To display the gas maps, we have chosen to consider as real a detection of emission when the amplitude over noise (hereafter A/N) of the line, defined as the fitted emission amplitude divided by the noise in the residual spectrum (galaxy spectrum − best fit over the whole SAURON range), is larger than 4 (see also Paper V and Paper VII). The bins below this threshold are displayed using a dark grey colour. Despite this cut in A/N, the gas detection covers in most cases a very large fraction of the SAURON field.

In NGC 4030 and 4102, we detected also significant emission from the [N I] doublet; however, in the large majority of our galaxies [N I] is very weak and hard to measure: since we would not learn more about our galaxies considering also the [N I] maps, we decided not to include them in Figs 5(a)–(r).

6.2 Stellar kinematics

All the objects show rotation, as expected. An interesting feature is the quite frequent central decline in σ (NGC 628, 772, 2805, 3346, 3949 and 5668). We measured also the higher moments h_3 and h_4, but unfortunately our spectra contain information only for the most early-type galaxies in our sample (NGC 488, 772, 4030 and 4102) which are generally the objects with the highest $(S/N)_\star$, where penalization does not play an important role (see Section 4.1 and Cappellari & Emsellem 2004). Some objects display misaligned photometric and kinematical axes (NGC 864, 3346 and 4487), a possible indication of non-axisymmetric structures such as bars. In other cases, the situation is less clear, due to the presence of twists in the rotation axis (NGC 772, 2964, 3949, 4254 and 5678). In many galaxies our measurements indicate very low velocity dispersions, as seen also on the basis of the central values reported in Table 1 and Fig. 1.

6.2.1 Radial behaviour of the stellar velocity dispersion

We addressed the radial behaviour of the stellar velocity dispersion σ by measuring the radial σ profiles and their slopes and correlating these with the morphological type. For each of our galaxies, we computed a σ profile by averaging the stellar velocity dispersion map on elliptical annuli orientated as the galaxy isophotes; for some strongly barred galaxies, the chosen orientation does not coincide with the position angle (PA) quoted in Table 1, which refers to the outermost isophotes. The ellipticity of the concentric ellipses is instead taken in all cases from Table 1. The distance between consecutive annuli is 0.8 arcsec along the minor axis, corresponding to the pixel size of the unbinned SAURON cubes. In order to take into account the galaxy size, we rescaled the radial coordinate by dividing it by the disc scalelength. The values for the disc scalelength h_r come from one-dimensional fitting of the photometric profiles that we extracted from space- and ground-based images via isophotal analysis. The details of this photometric analysis will be given in a future paper. We then estimated the σ gradient across the field by fitting a straight line to the data points by means of a least-squares algorithm. Fig. 6 illustrates the results. For each galaxy the computed σ profile is plotted against the scale-free radius r/h_r; the solid lines overplotted are the best-fitting straight lines, the slope of which is indicated in a corner of each panel. One can see that for some galaxies a straight line is clearly not an optimal description of the data, at least not over the whole radial range considered, but it serves as an indication of a global trend. The dotted line drawn on each plot marks the $r = 1.2$ arcsec line, which represents the edge of the squared aperture within which the central σ values reported in Table 1 were computed. In Fig. 7, we plot the slope of these scale-free fits against the morphological type of the galaxy. A weak global trend can be recognized: the slope tends to increase with later types, indicating that it is more probable for later-type galaxies to have a central region colder than the surroundings, rather than a hotter one. In the figure, we labelled with (B) the galaxies classified as barred (B and AB in Table 1), but we do not detect any significant correlation with bar classification.

The velocity-dispersion profile is determined by the mass distribution of the galaxy, the anisotropy of the velocity distribution and the viewing angle. Galaxies with more concentrated light distribution will have larger central peaks in their σ profiles. Elliptical galaxies generally have σ profiles decreasing outwards (see e.g. D'Onofrio et al. 1995), and this is also the case for many early-type spirals (Paper VII), as a result of a centrally concentrated bulge. Here, we see that for the later type spiral galaxies there is no sign anymore in the σ profile of this central mass concentration, which is indeed expected for galaxies with lower bulge/disc ratios: for later types bulges are smaller and have lower surface brightness (see e.g. Falcón-Barroso et al. 2002). In some cases, however, we see that σ is increasing outwards, which is a sign of cooler central mass concentration. Emsellem et al. (2001), Márquez et al. (2003), Shapiro et al. (2003) and Paper VII have shown that these central σ-drops are quite common, and are in general associated with disc-like

[5] We used WFPC2 images taken with the F606W filter for NGC 488, 628, 864, 1042, 2964, 3423, 3949, 4030, 4102, 4254, 4487, 5585 and 5678 and with the F814W filter for NGC 2805, 3346, 4775 and 5668.

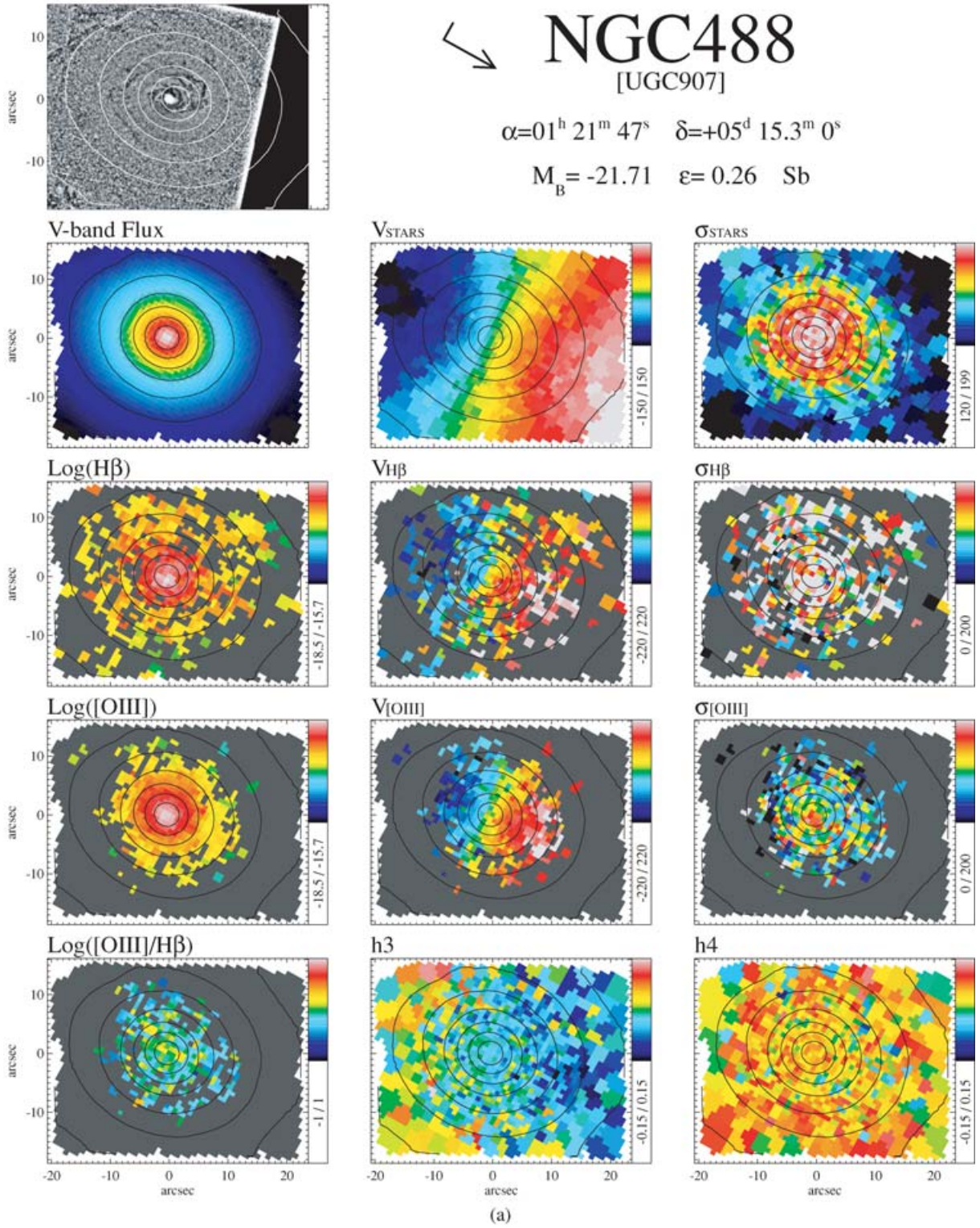

Figure 5. (a) Maps of stellar and gaseous kinematics for NGC 488. First row: unsharp-masked image and some astrometric information; second row: stellar flux (in mag arcsec^{-2}, with an arbitrary zero-point), velocity and velocity dispersion (in km s^{-1}); third and fourth row: respectively Hβ and [O III] fluxes (in erg s^{-1} cm^{-2} and logarithmic scale), velocity and velocity dispersion (in km s^{-1}); fifth row: [O III]/Hβ line ratio (in logarithmic scale), stellar h_3 and h_4 moments. The ranges are indicated in the box on the right-hand side of each map. In the gas maps, the dark grey colour is used for the bins with A/N below the selected threshold. (b) As in Fig. 5(a) for NGC 628. (c) As in Fig. 5(a) for NGC 772. (d) As in Fig. 5(a) for NGC 864. (e) As in Fig. 5(a) for NGC 1042. (f) As in Fig. 5(a) for NGC 2805. (g) As in Fig. 5(a) for NGC 2964. (h) As in Fig. 5(a) for NGC 3346. (i) As in Fig. 5(a) for NGC 3423. (j) As in Fig. 5(a) for NGC 3949. (k) As in Fig. 5(a) for NGC 4030. (l) As in Fig. 5(a) for NGC 4102. (m) As in Fig. 5(a) for NGC 4254. (n) As in Fig. 5(a) for NGC 4487. (o) As in Fig. 5(a) for NGC 4775. (p) As in Fig. 5(a) for NGC 5585. (q) As in Fig. 5(a) for NGC 5668. (r) As in Fig. 5(a) for NGC 5678.

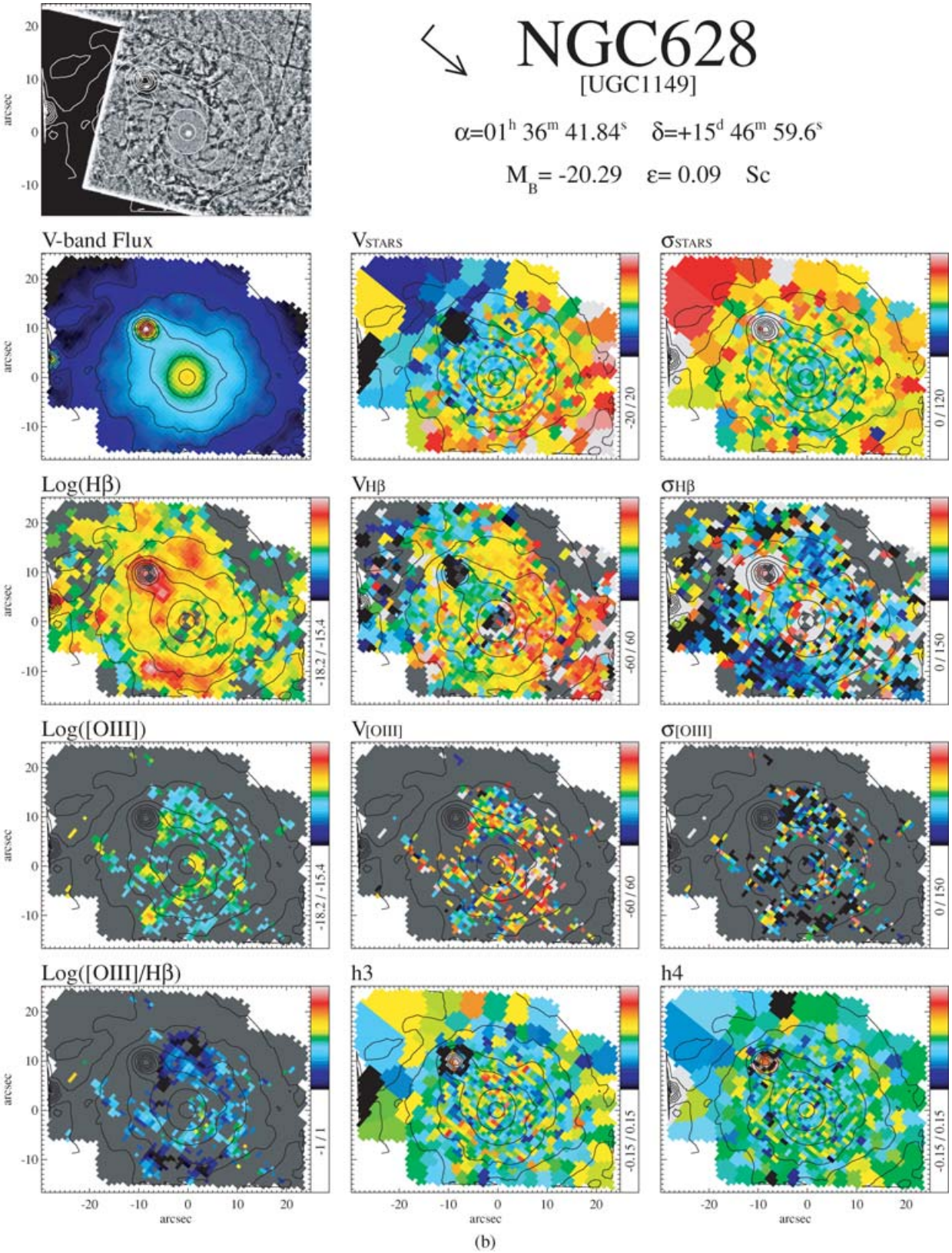

Figure 5 – *continued*

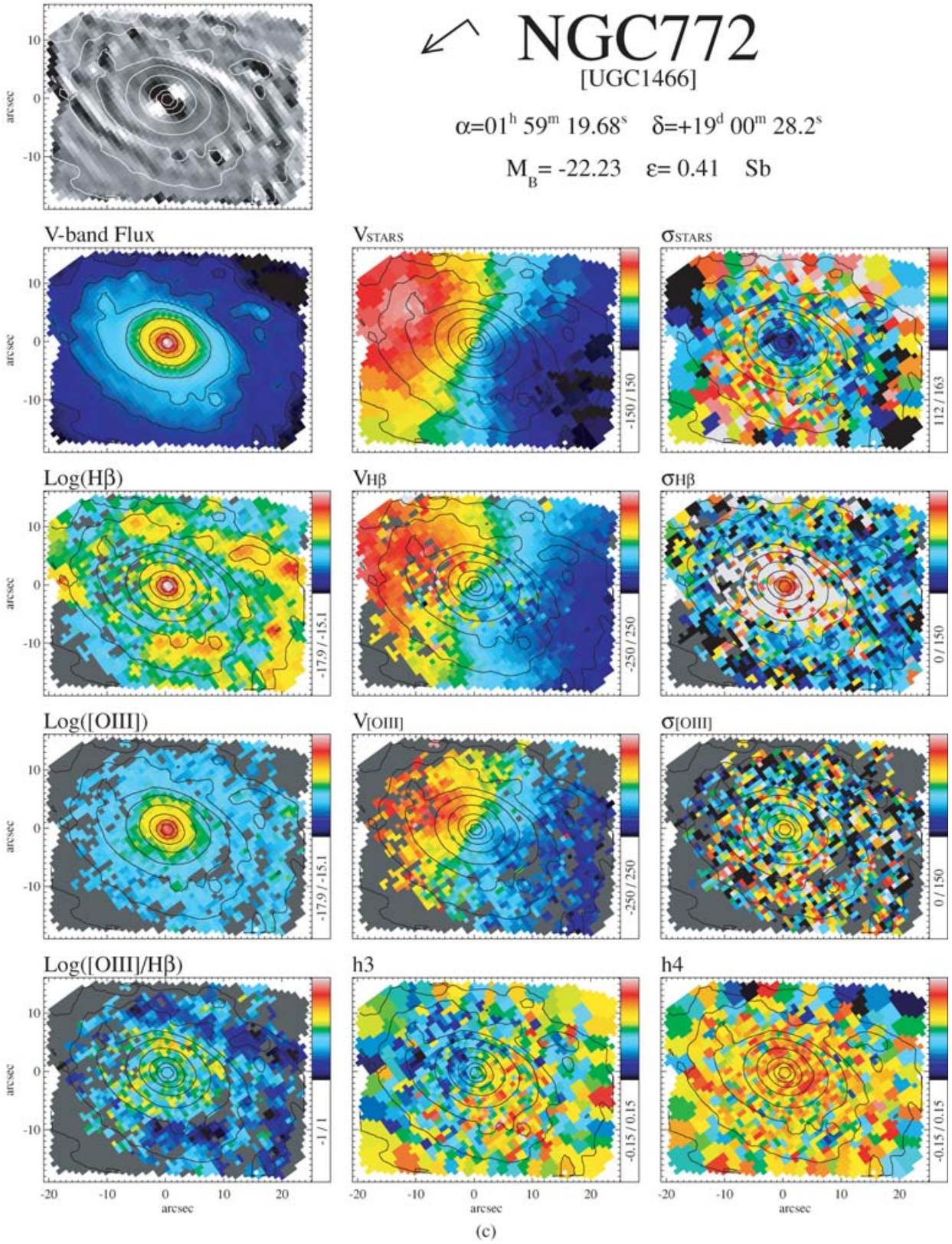

Figure 5 – *continued*

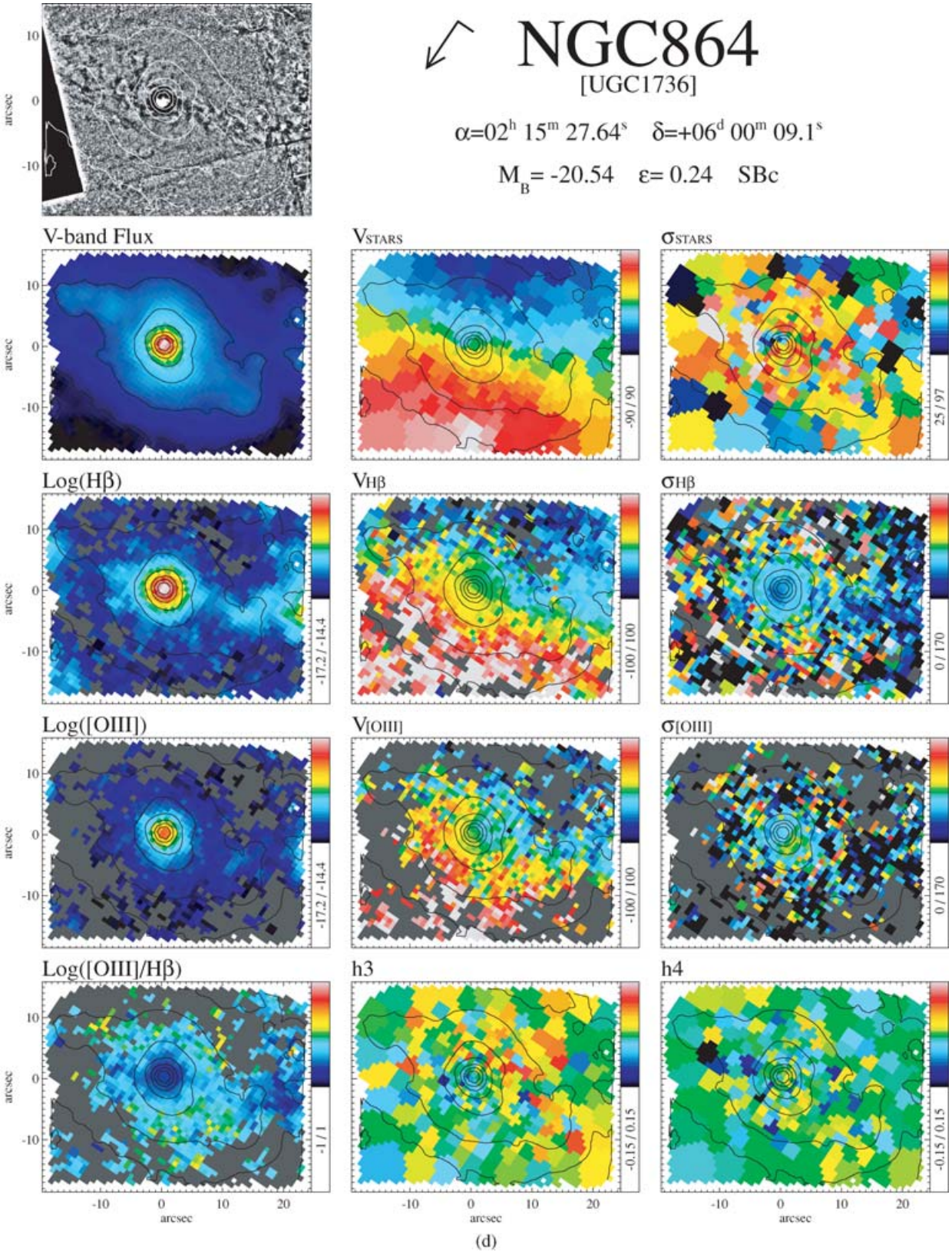

Figure 5 – *continued*

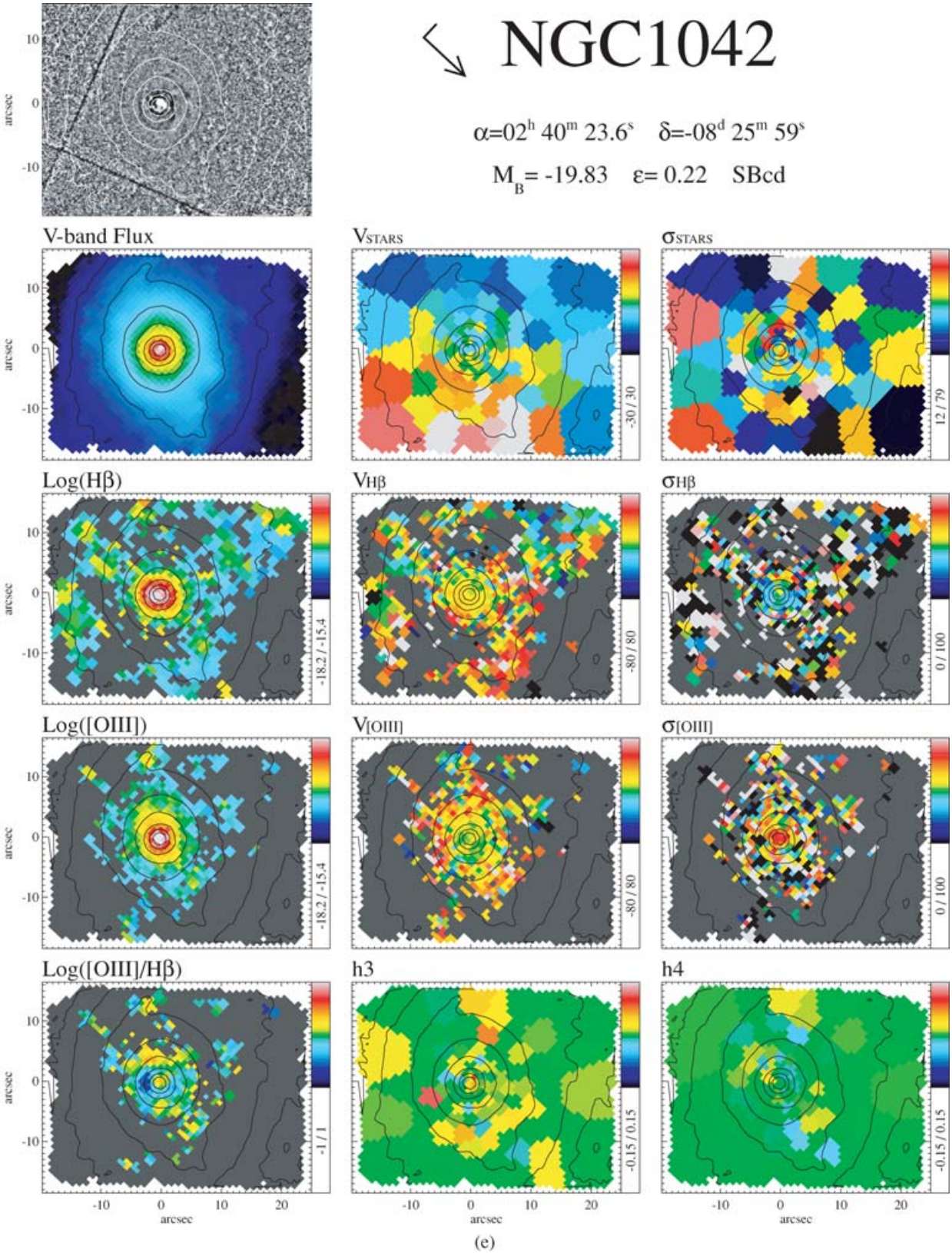

Figure 5 – *continued*

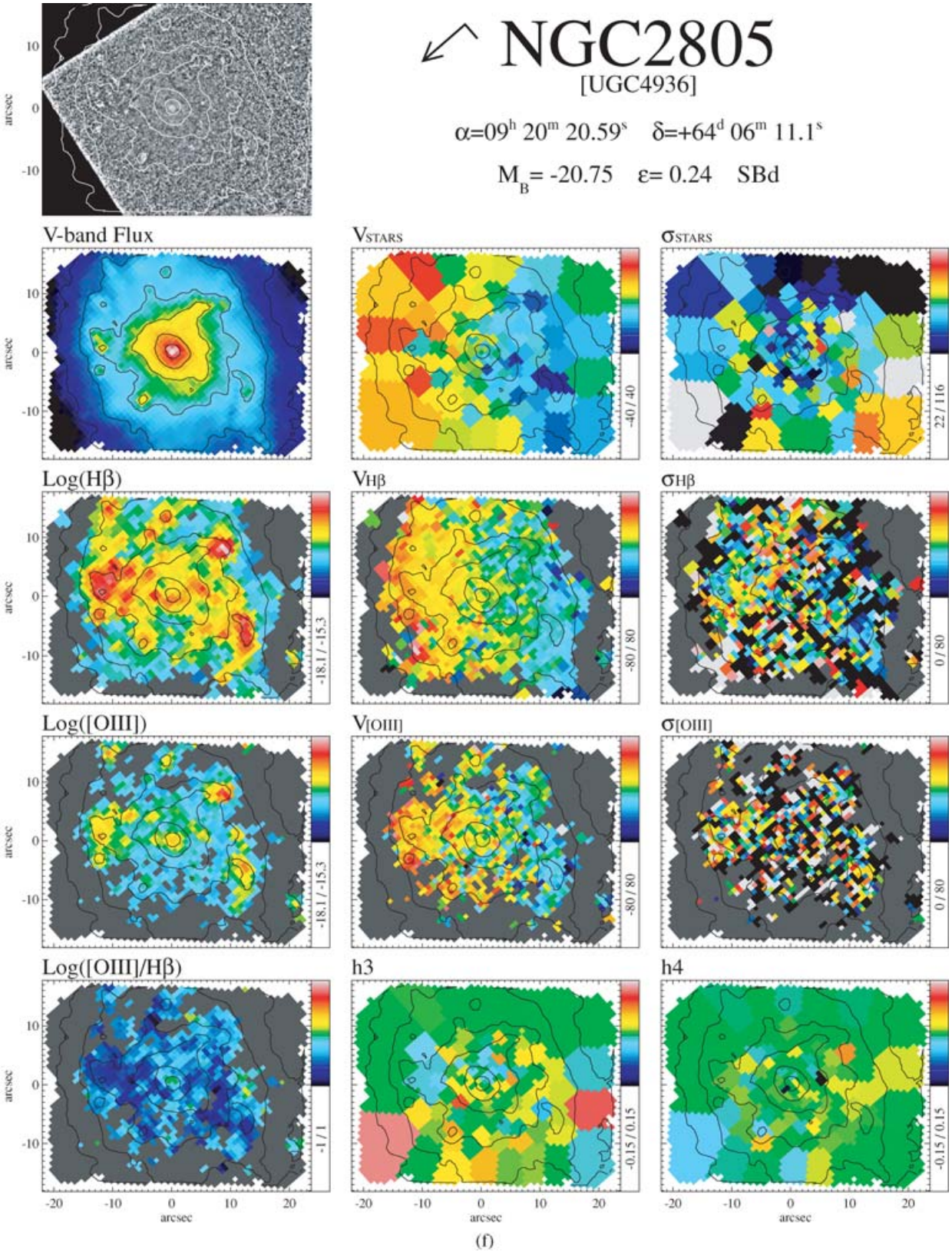

Figure 5 – *continued*

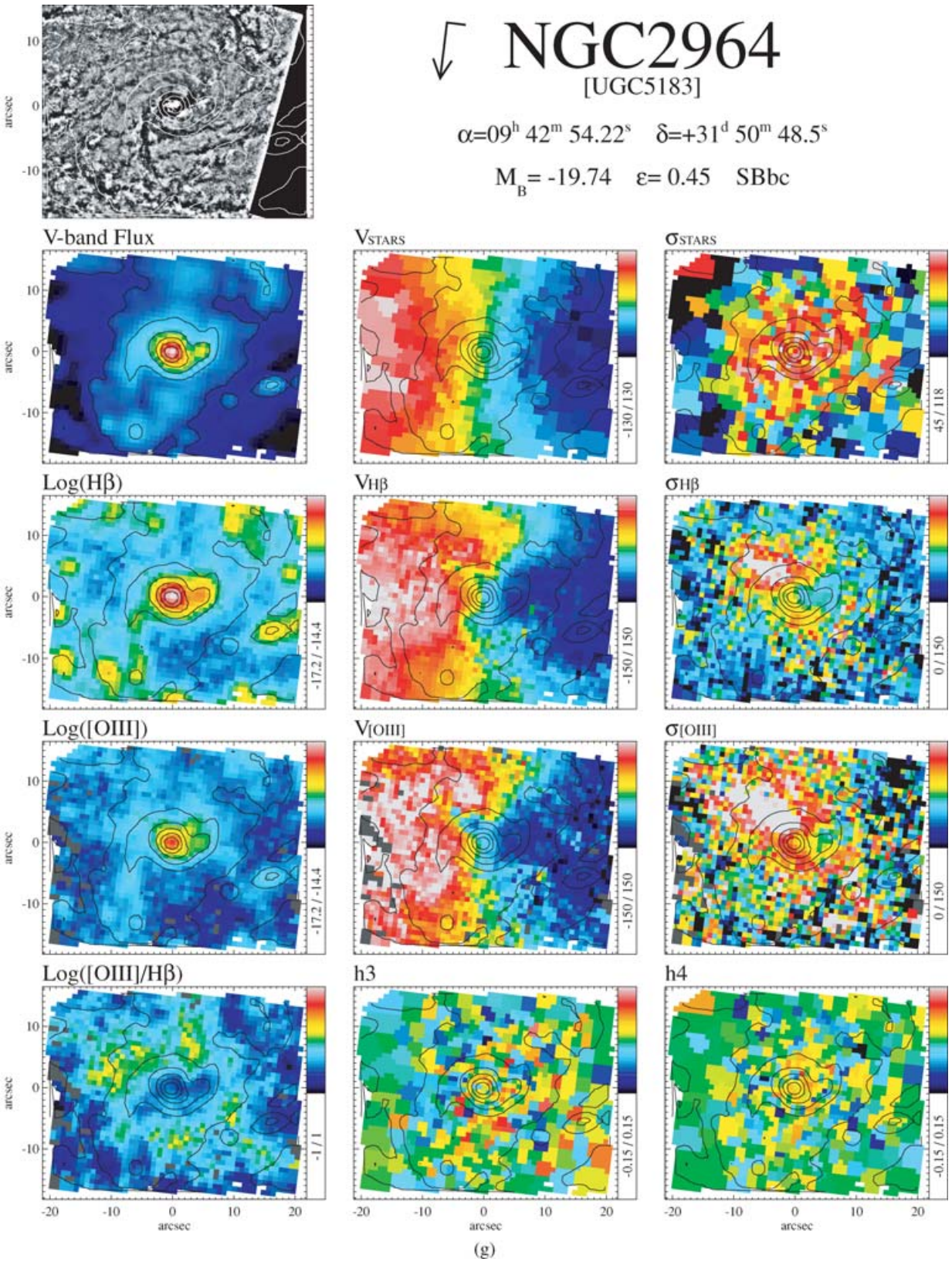

Figure 5 – *continued*

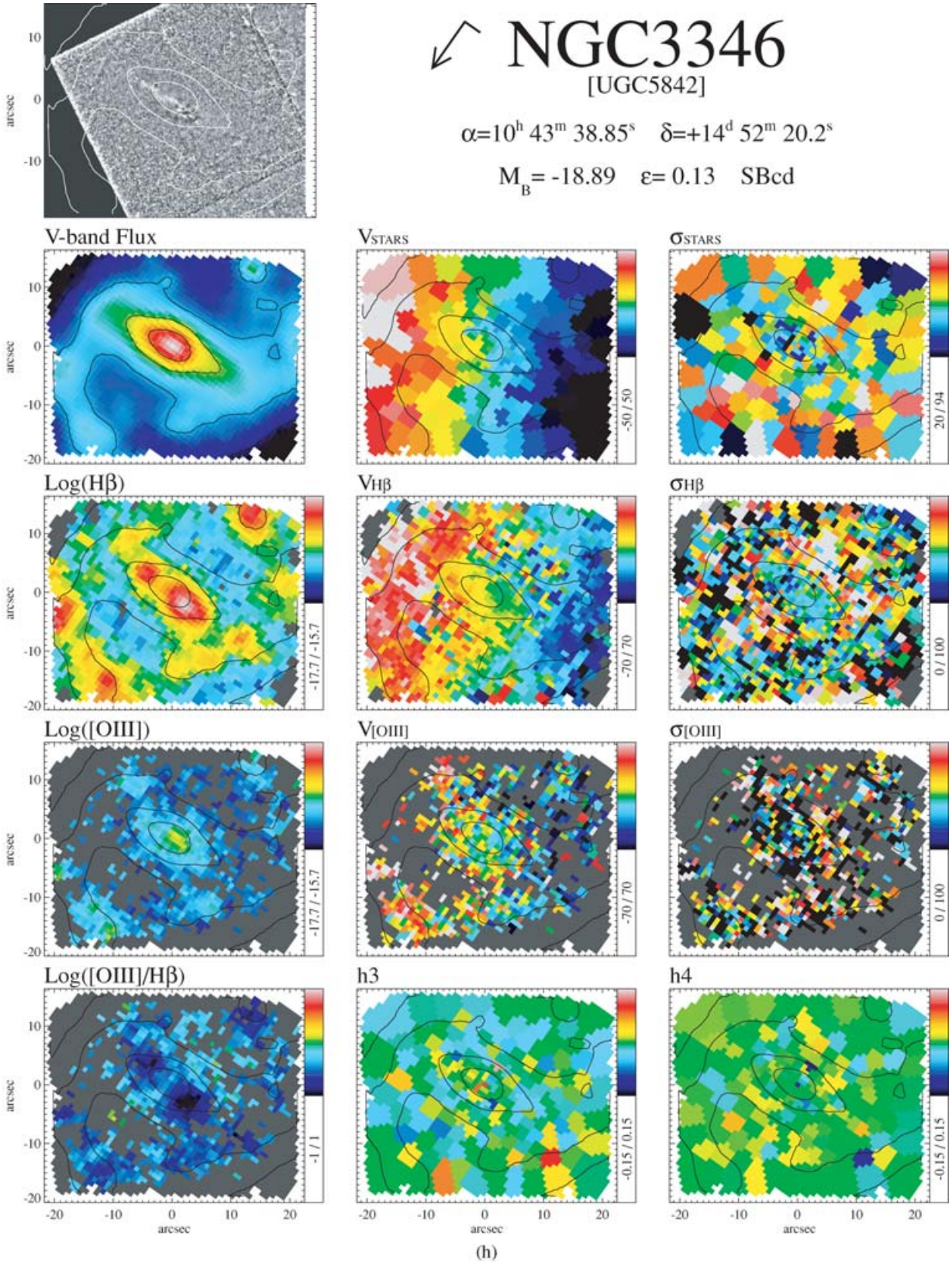

Figure 5 – *continued*

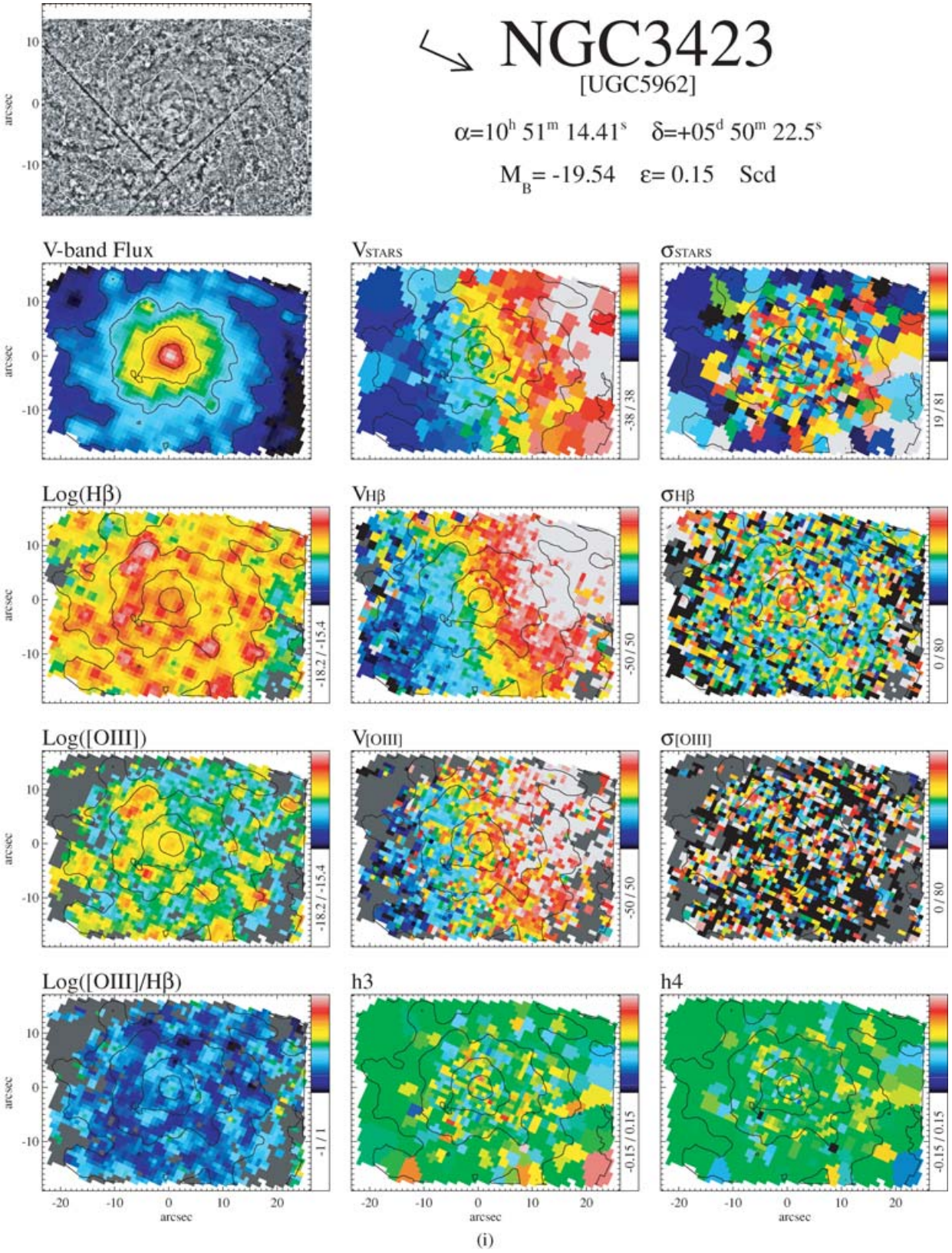

Figure 5 – *continued*

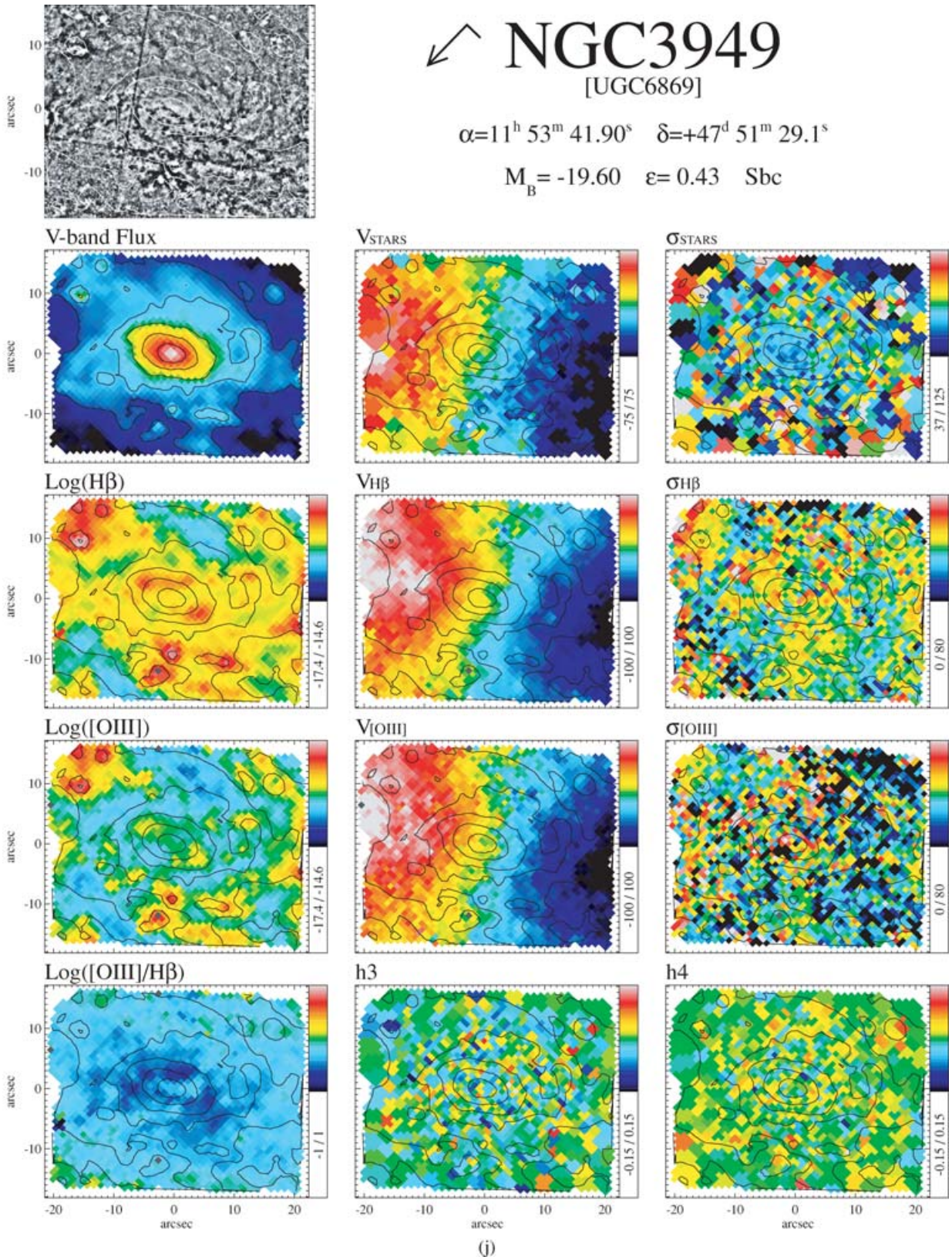

Figure 5 – *continued*

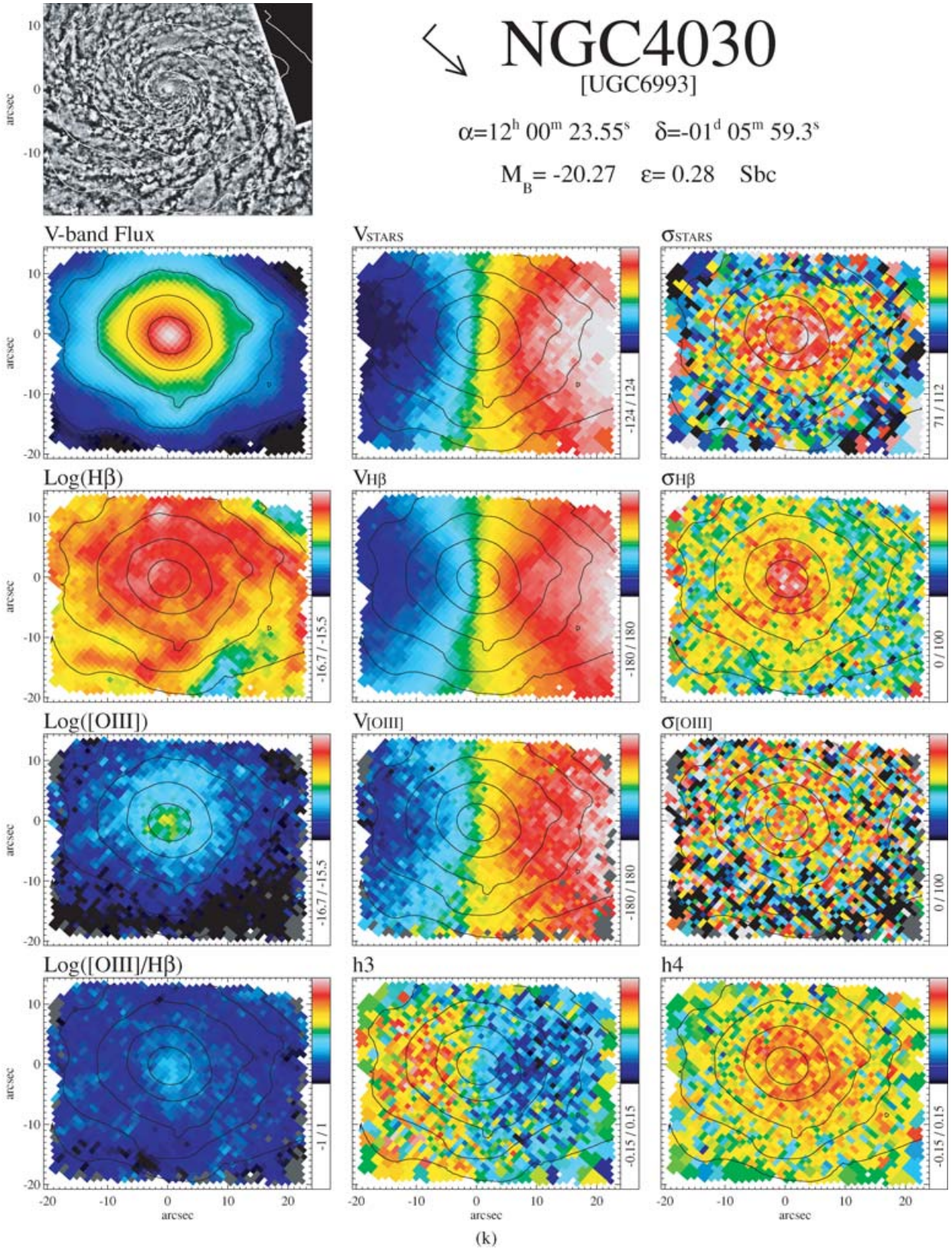

Figure 5 – *continued*

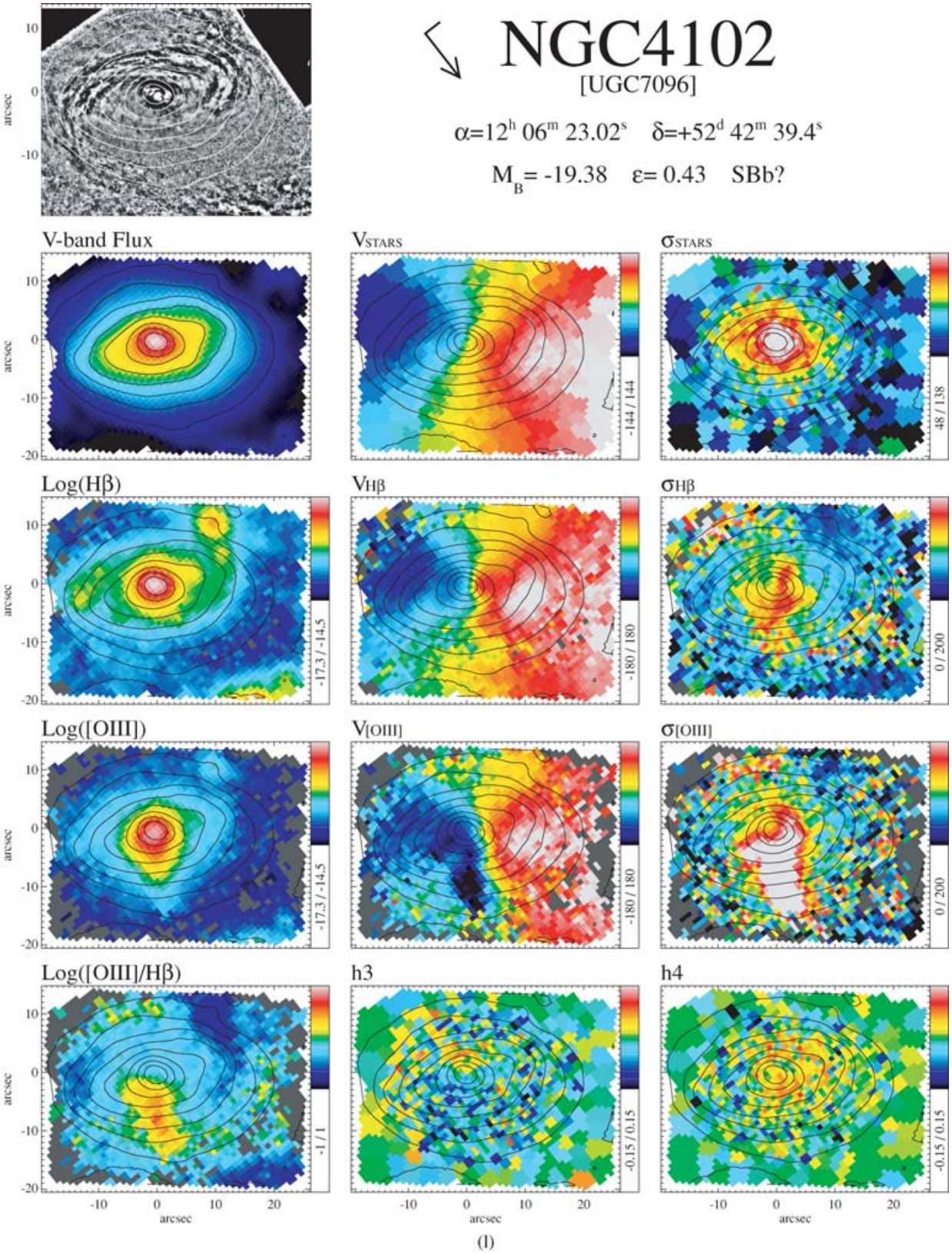

Figure 5 – *continued*

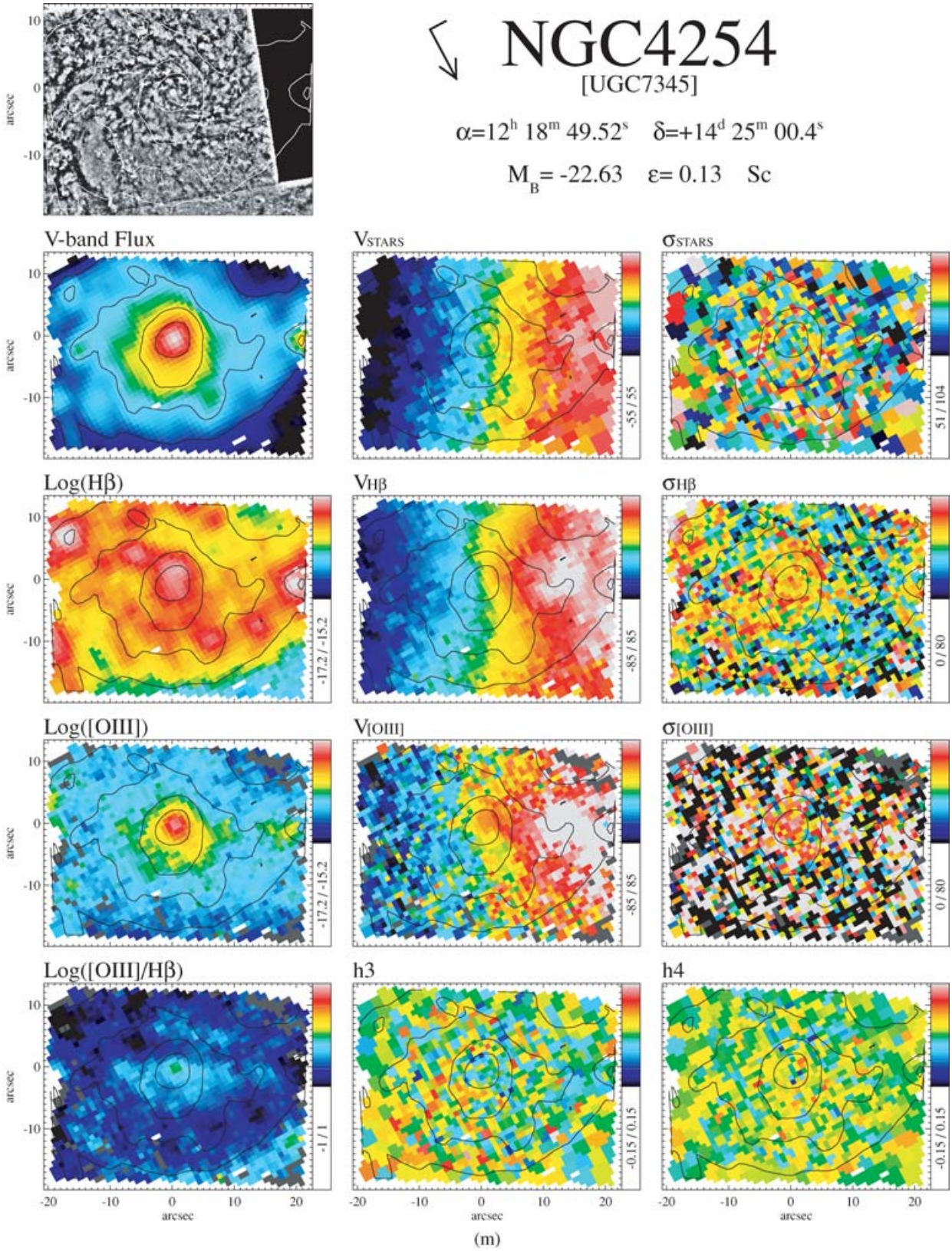

Figure 5 – *continued*

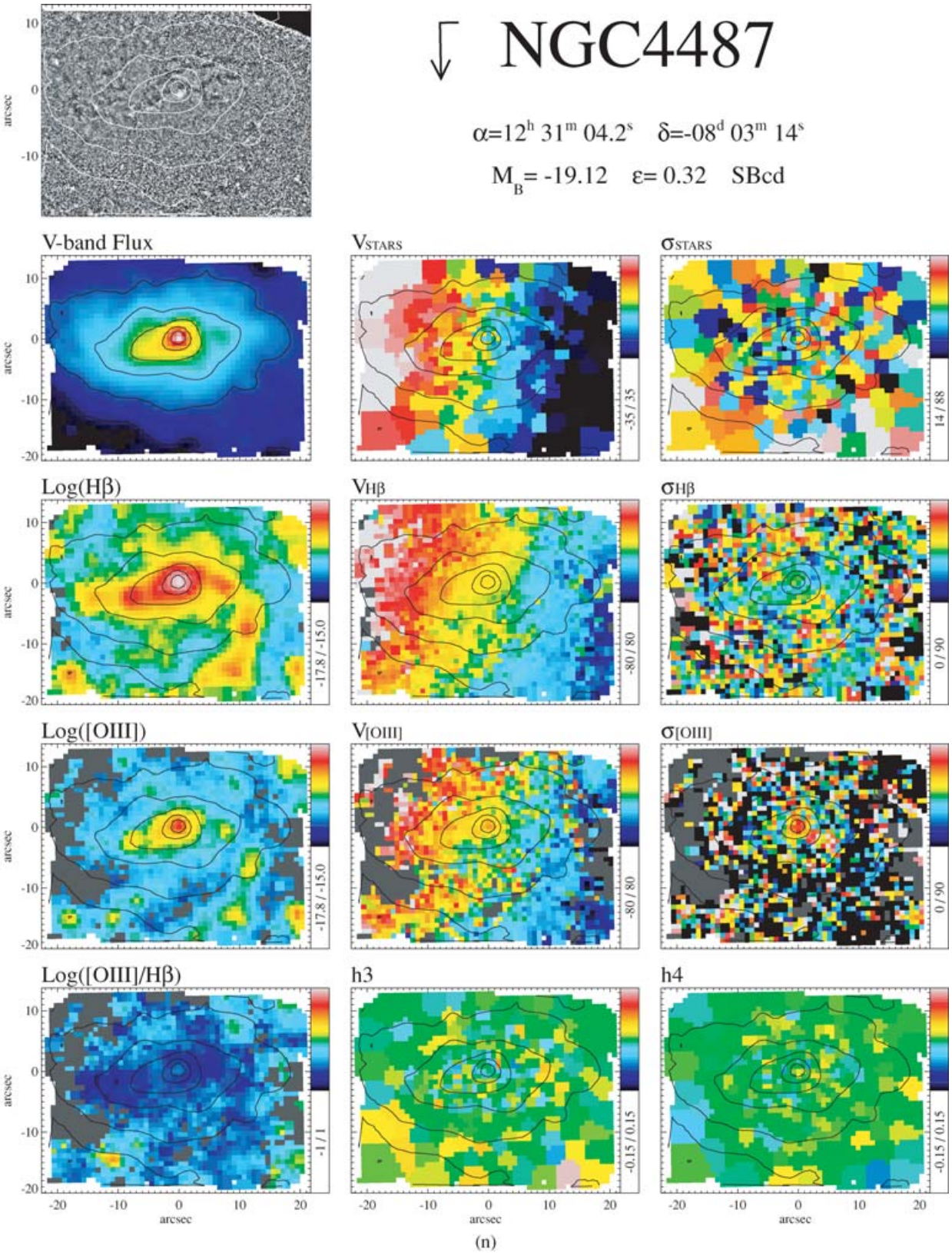

Figure 5 – *continued*

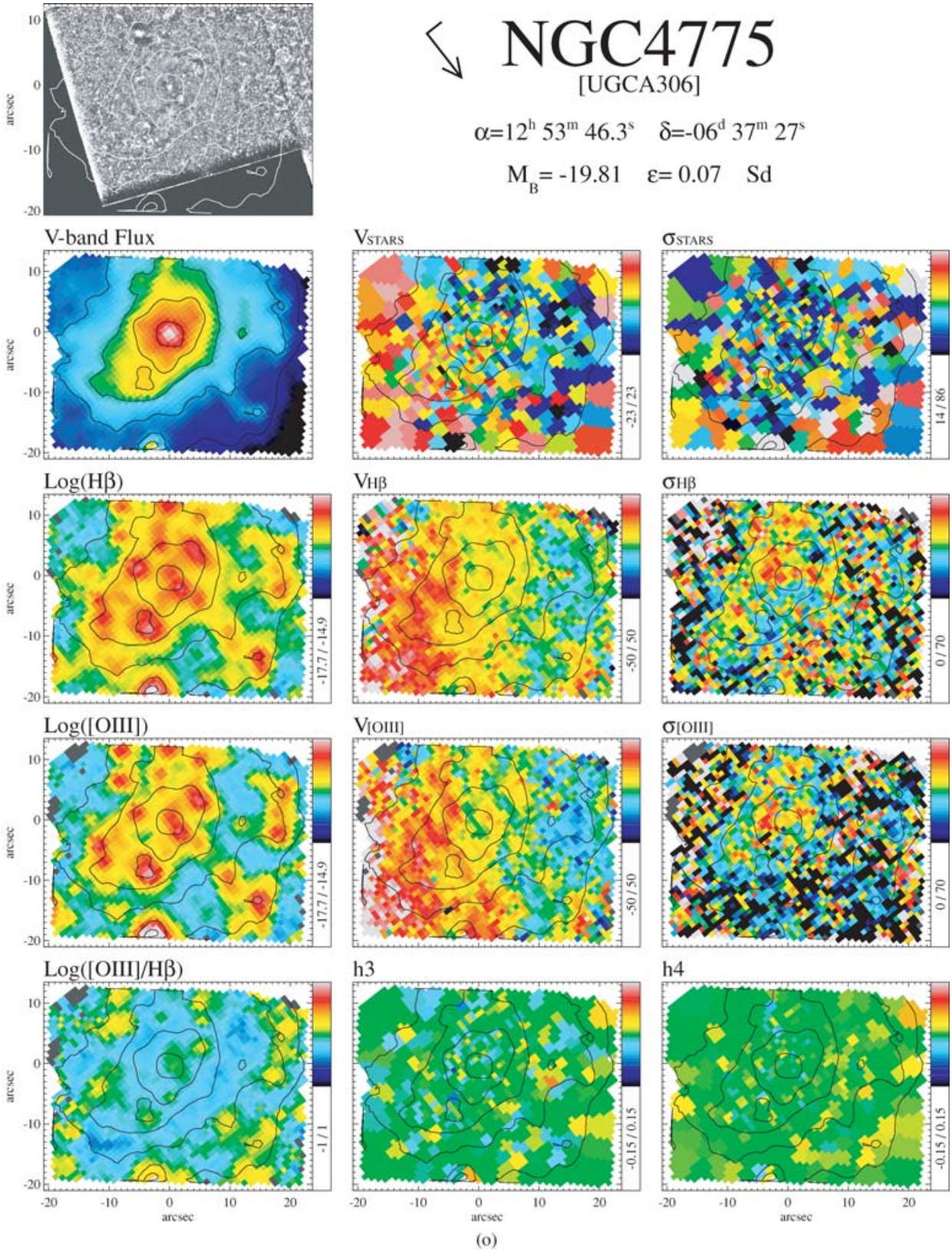

Figure 5 – *continued*

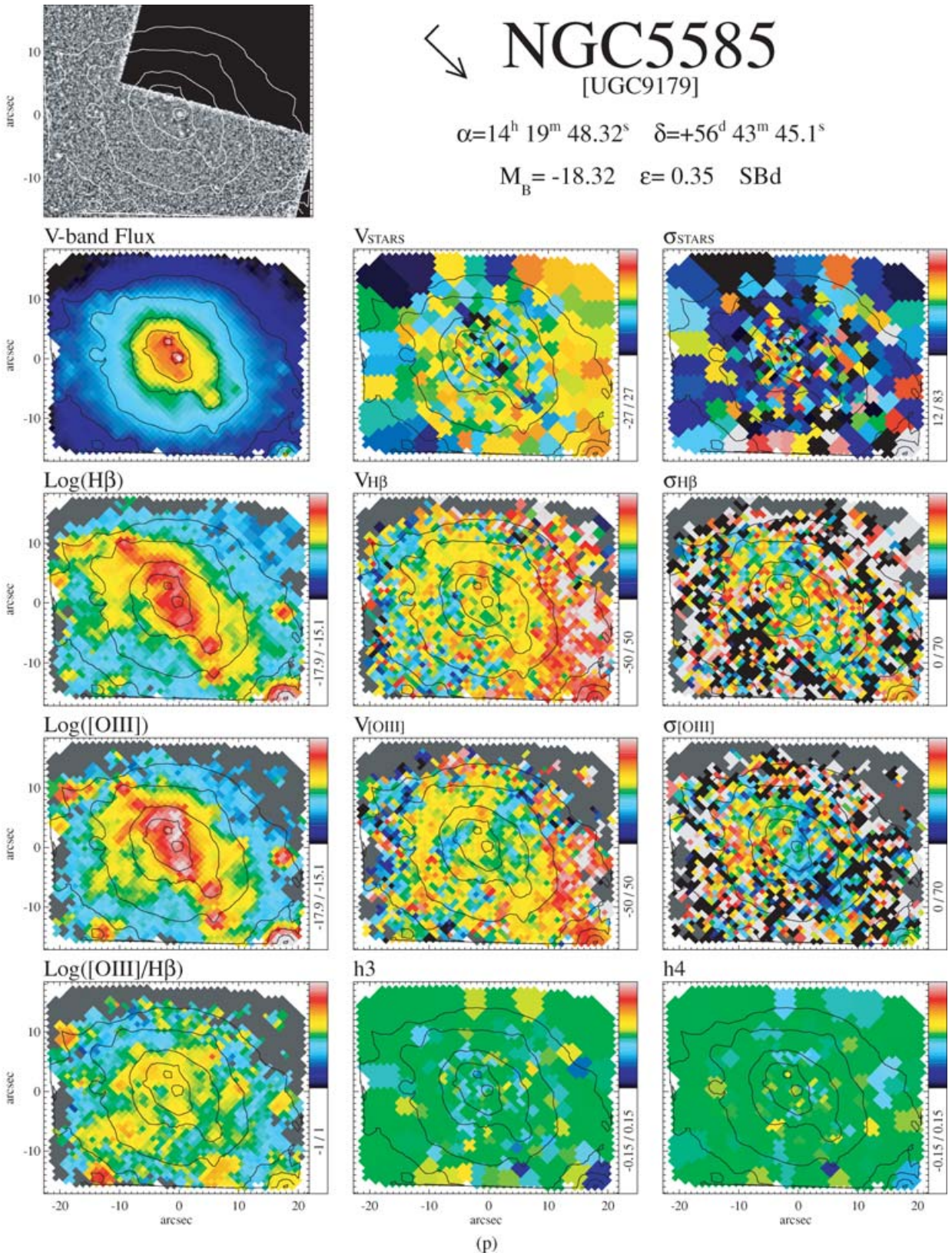

Figure 5 – *continued*

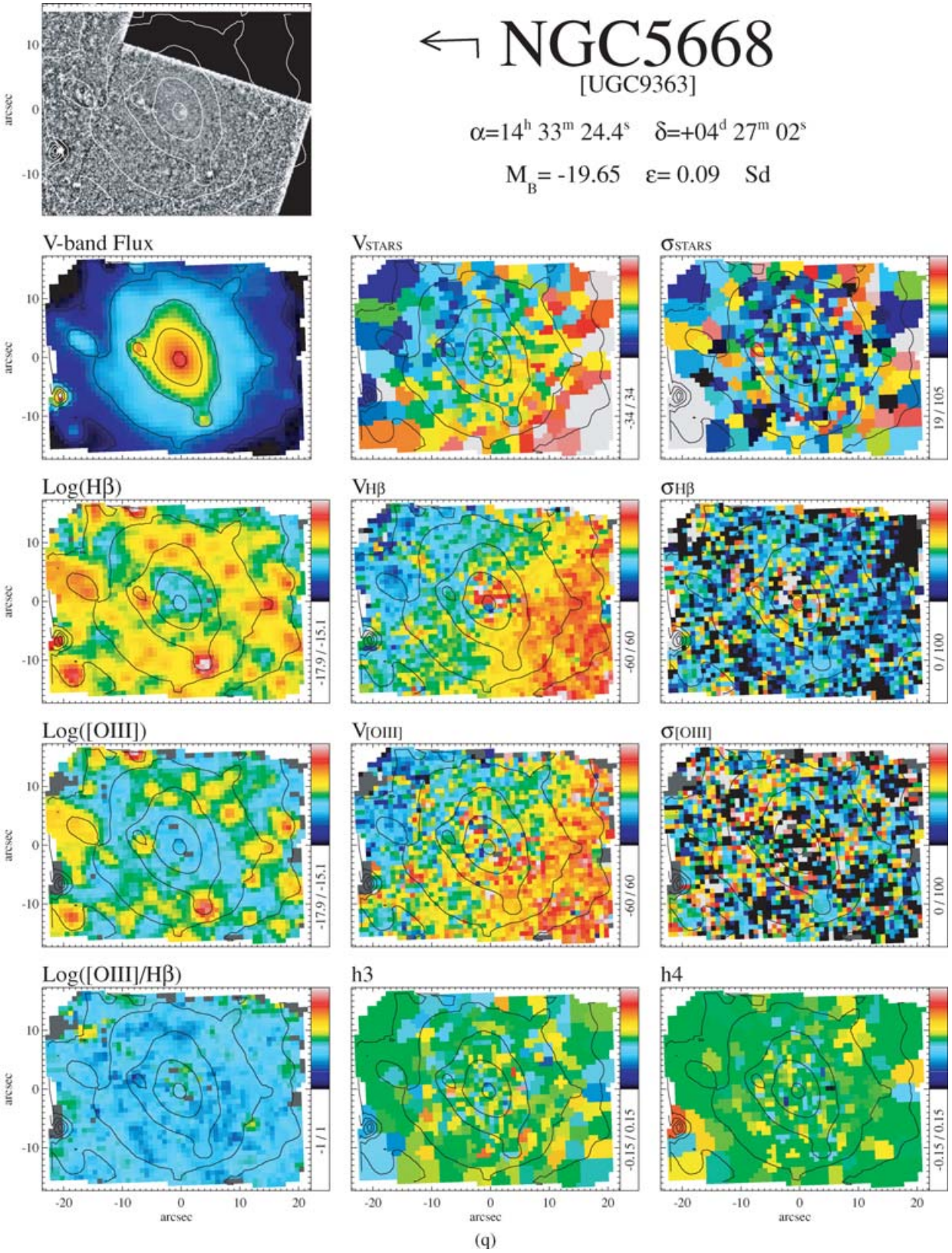

Figure 5 – *continued*

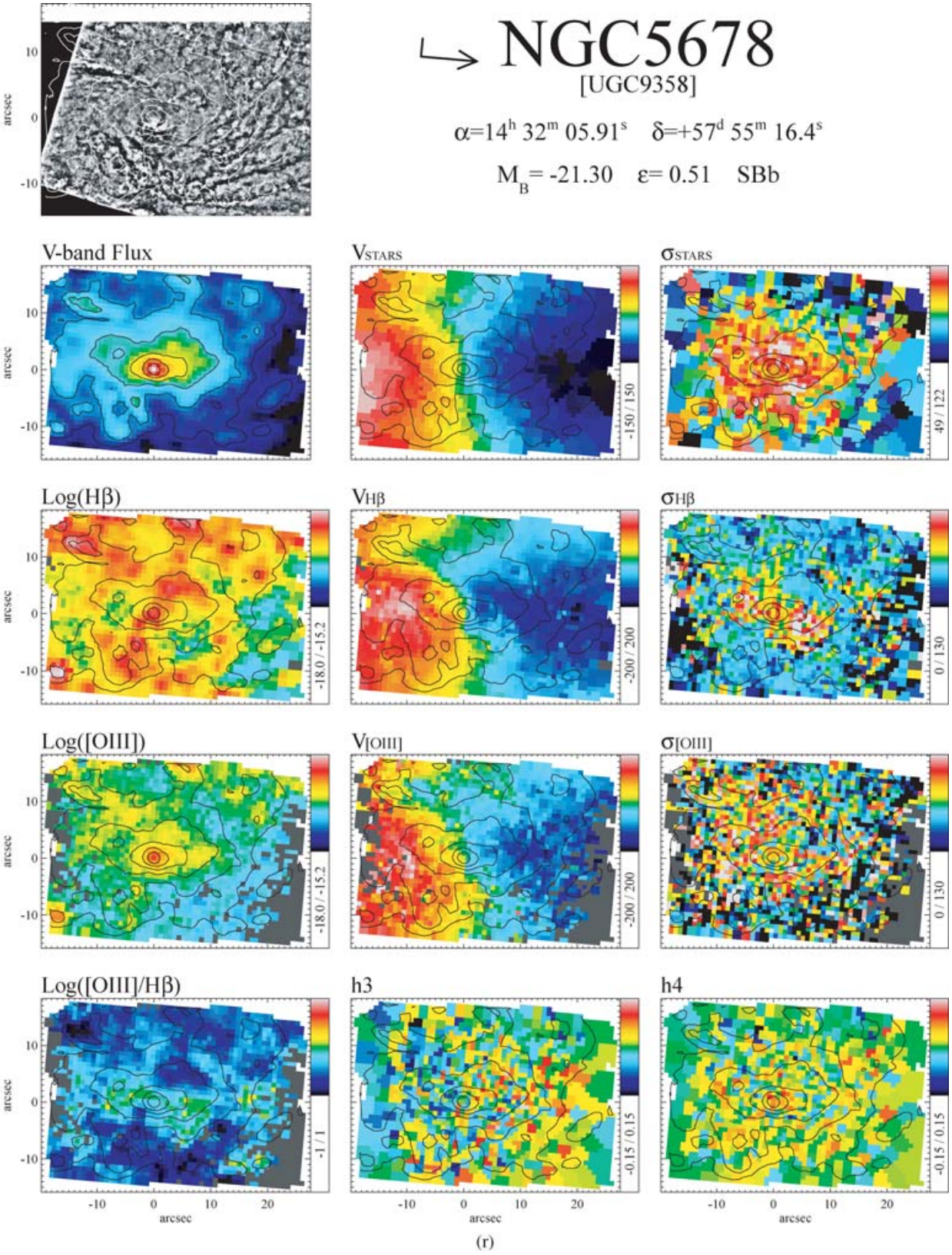

Figure 5 – *continued*

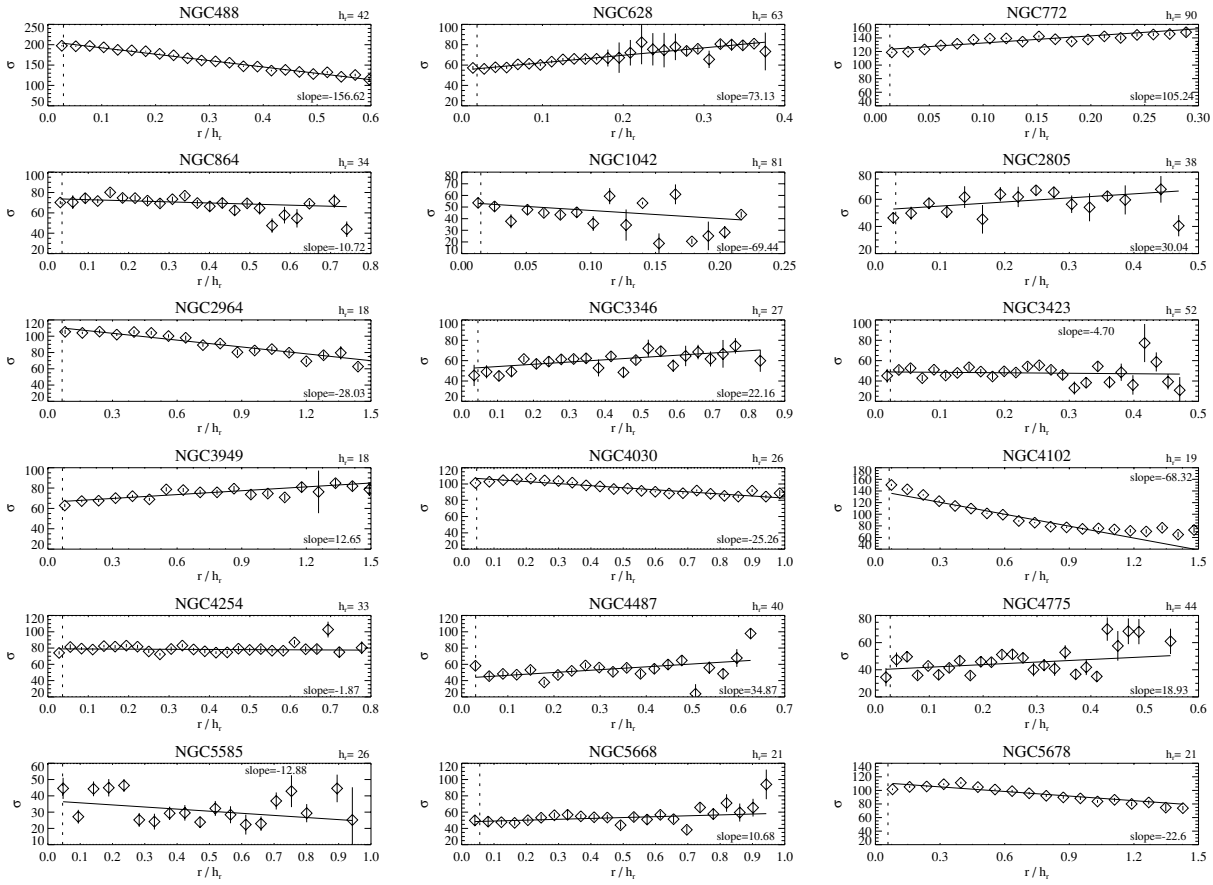

Figure 6. The plots present galaxy by galaxy the radial profile of stellar velocity dispersion (in km s^{-1}), calculated on elliptical annuli as explained in the text; on the horizontal axis we plot a scale-free radius, obtained dividing our radial coordinate (semimajor axis of the ellipses in arcsec) by the disc scalelength h_r (also expressed in arcsec and written above each plot). A straight line is fitted to the velocity dispersion profiles; the solid lines overplotted are the best-fitting straight lines, the slope of which is recorded in a corner of each panel; the dotted vertical line indicates in each panel the $r = 1.2$ arcsec line within which the central values of Table 1 were calculated.

structures. They are most likely due to stellar discs formed from gas that has been accreted towards the centre. This is in agreement with simulations by Wozniak et al. (2003). Our measurements show that also galaxies as late as Sd present velocity dispersion drops. The fact that the velocity dispersion profiles are flat or rising does not necessarily mean that these galaxies have no bulge – by detailed modelling in a future paper we will be able to answer this question.

6.2.2 Qualitative comparison with HST photometry

It is not straightforward to connect our kinematic results with photometry. In the last decade, analysis based on *HST* imaging (Carollo et al. 1997, 1998; Peletier et al. 1999; Böker et al. 2002; Carollo et al. 2002; Laine et al. 2002) revealed that late-type galaxies do not necessarily possess classical bulges[6]; they can instead host small-scale structures such as nuclear bars, nuclear star clusters, point-like sources. We cross-correlated the above-mentioned samples with our own and tried to look for kinematical signatures of the photometric features that they detected in the images. In Table 3 we tabulate the results of this comparison, based on a review of the relevant literature, on the appearance of our maps [Figs 5(a)–(r), Section 6.1] and of the radial behaviour of σ as well (Fig. 6).

According to Böker et al. (2002), NGC 1042, 2805, 3346, 3423, 4487, 4775, 5585 and 5668 host a nuclear star cluster and do not have a stellar bulge; our data show that the central regions of these objects are indeed cold. For any speculation on nuclear star clusters, caution is needed, since the nuclear star clusters detected with *HST* imaging have a spatial scale usually much smaller than the SAURON resolution. There are also cases where our observations nicely support the photometrical results: NGC 488 has a classical $r^{1/4}$ bulge (Carollo et al. 1997), and our maps show a hot, extended central region; NGC 4030 has also a large stellar bulge – although classified as 'irregular' and 'exponential' (Carollo et al. 1998) – and our data show a hot nuclear region. To conclude, the examples show that there is a correspondence between the photometric lack of a stellar bulge and the kinematical measurement that the inner regions are cold. At the moment this is a qualitative statement that requires further investigation. As previously stated, in a future paper we will study deeper the relation between the kinematical structures and the shape of the photometrical profiles.

[6] We note here that Carollo et al. (1997, 1998, 2002) refer to a definition of classical bulge as a centrally concentrated stellar distribution with an amorphous, smooth appearance. This implicitly excludes gas, dust and continuing recent star formation (Wyse, Gilmore & Franx 1997).

6.3 Gas kinematics

In our data, the gas rotates usually faster than the stars and around the same axis; the gas velocity fields are much more complicated

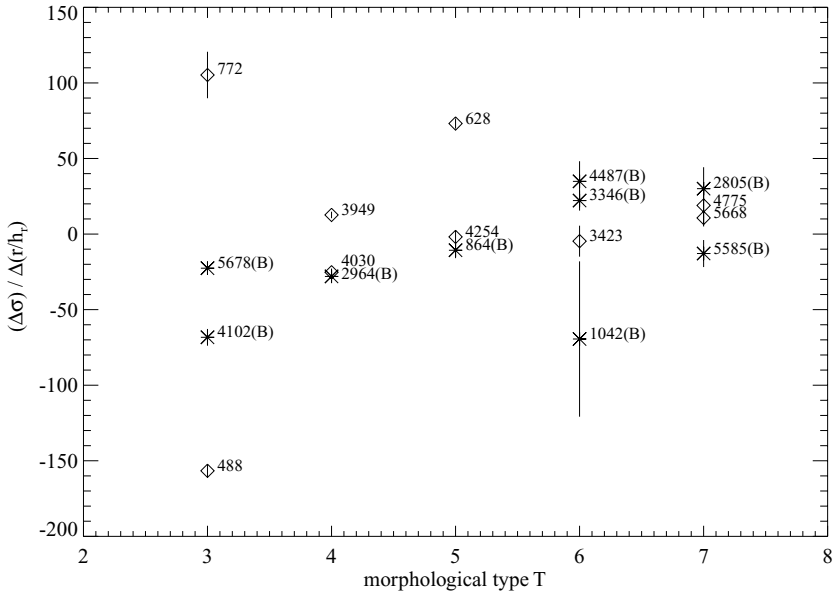

Figure 7. The fitted slope $\Delta\sigma/\Delta(r/h_r)$ of the velocity dispersion profiles is plotted here as a function of morphological type; the values for this slope are those indicated in the panels in Fig. 6. The galaxies classified as barred are here labelled with (B) and represented by asterisks; the NGC galaxy identifiers are indicated close to the corresponding symbol.

Table 3. Comparison with *HST* photometry. References in the table: C97, Carollo et al. 1997; C98, Carollo et al. 1998; C02, Carollo et al. 2002; B02, Böker et al. 2002. Abbreviations: $r^{1/4}$b, de Vaucouleurs bulge; irb, irregular bulge (when a galaxy possess a central dense component but does not have a featureless appearance); expb, exponential bulge; nuc, nuclear compact source; nsc, nuclear star cluster; sf, nuclear star forming region. For a more accurate description of the photometric features, we refer the reader to the quoted papers.

NGC	*HST*	References	SAURON
488	$r^{1/4}$b	C97	Hot central region
1042	nsc	B02	Low σ over the field
2805	nsc	B02	Cold central region
2964	sf, nuc	C97, C02	σ enhanced in the centre
3346	nsc	B02	Cold central region
3423	nsc	B02	Low σ over the field
3949	nuc	C02	Cold central region
4030	irb, expb	C98	Hot central region
4102	irb	C97	Hot central region
4487	nsc	B02	Cold central region
4775	nsc	B02	Low σ over the field
5585	nsc	B02	Low σ over the field
5668	nsc	B02	Cold inner region
5678	nuc	C02	Hot central region

Table 4. The table reports galaxy by galaxy the decimal logarithm of the global fluxes in the Hβ and [O III] emission lines, in erg s^{-1} cm^{-2}.

NGC	log FHβ	log F[O III]	NGC	log FHβ	log F[O III]
488	−13.72	−13.79	3949	−12.32	−12.59
628	−13.34	−14.12	4030	−12.51	−13.18
772	−13.18	−13.59	4102	−12.69	−12.85
864	−13.03	−13.53	4254	−12.48	−13.13
1042	−13.84	−13.92	4487	−12.91	−13.40
2805	−13.32	−13.84	4775	−12.64	−12.70
2964	−12.60	−13.03	5585	−12.98	−12.89
3346	−13.47	−14.14	5668	−12.89	−13.15
3423	−12.93	−13.45	5678	−12.80	−13.33

than the stellar ones, with zero-velocity lines that are often wiggling, inclined or S-shaped (NGC 772, 2964, 3346, 3949, 4102, 4254 and 5678). When comparing the results in the two diagnostic lines (Hβ and [O III]), we notice that in many cases the Hβ distribution is spatially more extended than the [O III] one (NGC 488, 628, 864, 1042, 2805 and 3346) and that the flux in Hβ is in most cases higher than in [O III], although there can be specific regions where the situation is opposite, with less emission in Hβ rather than in [O III], which is the case for NGC 4102 and 5585. In Table 4 we list the total Hβ and [O III] fluxes, obtained summing the line fluxes in all the bins that meet the A/N criterion. There are generally no major differences between the velocity fields in the two lines, while the velocity dispersion is usually higher in Hβ; exceptions to this statement will be highlighted in the description of the individual galaxies (Section 6.4). The differences between the two lines are particularly strong in the case of NGC 4102 (see also Fig. 3 and the related text), which is classified as a low-ionization nuclear emission-line region (LINER). Overall, the sample galaxies display low [O III]/Hβ ratios over most of the SAURON field, suggesting star formation, as expected in spiral galaxies.

6.4 Notes on individual galaxies

Here, we comment individually on the galaxies of our sample; for each of them, we first summarize the known properties from previous work, then we describe the most interesting features seen in our SAURON maps, shown in Section 6.1.

6.4.1 NGC 488

NGC 488 is the most 'elliptical-like' galaxy in our sample; it is an unbarred Sb galaxy with a very regular tightly wound spiral pattern, with a pitch angle of only 5° (Kormendy 1984; Gerssen,

Kuijken & Merrifield 1997), and a large and smooth central bulge. According to Carollo et al. (1997), this is a classical $r^{1/4}$ bulge. The rotation curve has been measured using Hα and [N II]6583 Å data by Peterson (1980) out to a radius of 20 kpc, where he found that the velocity reaches $\approx$363 km s^{-1}, and continues to increase outwards. This galaxy has been studied using photometric and kinematic data to construct a dynamical model of bulge and disc (Fuchs 1997), concluding that the disc is dynamically cold.

The SAURON maps show regular stellar and gaseous rotation, with stars and gas rotating fast around the photometric minor axis and stellar velocity dispersion smoothly increasing towards the centre (consistent with the presence of the large bulge), to reach the highest value in our sample (around 200 km s^{-1}, see also Table 1 and Fig. 6). The gas turns out to be quite patchy (Hβ) and centrally concentrated.

6.4.2 NGC 628

NGC 628, also known as M74, is a well-studied grand-design spiral galaxy classified as Sc. It is known to be surrounded by an elliptical ring of neutral hydrogen extending well beyond the optical disc, out to $\approx 3R_{H_0}$ (isophotal radius at the 26.5 mag arcsec^{-2} surface brightness level), lying in a plane which is $\approx 15^\circ$ inclined with respect to the plane of the bright inner disc (see Roberts 1962; Briggs et al. 1980; Briggs 1982). The origin of the warped velocity field of the outer galaxy has been debated, since the apparent isolation of this galaxy makes it difficult for tidal disruption to be responsible for the warp. UV observations of NGC 628 have shown spiral arms with a more symmetrical appearance than in the optical; Chen et al. (1992) identified in the UV a possible companion 7.6 arcmin south-west from the nucleus, which could have helped to clarify the origin of the outer warp, but later it turned out to be a spurious detection. From both near-infrared (NIR) spectroscopy of CO absorption and submillimetric imaging of CO emission, a circumnuclear ring of star formation has been seen (Wakker & Adler 1995, James & Seigar 1999). These rings are believed to exist as a result of a barred potential; Seigar (2002) claims that ground-based NIR images suggest the presence of an oval distortion at $\approx$2 kpc from the centre, which could be part of the dissolution of a bar and responsible for the circumnuclear ring. On the basis of their analysis of *HST H*-band images, Laine et al. (2002) found a bar on a $\approx$100-pc scale; this would then be a case of nested bars.

From the stellar population side, Cornett et al. (1994) concluded that the star formation history of NGC 628 varies with galactocentric distance; Natali, Pedichini & Righini (1992) suggested that the galaxy could be seen as an inner and an outer disc characterized by different stellar populations; according to them, the transition between the two regions is located at $\approx$8–10 kpc from the centre.

NGC 628 can be resolved from the ground into individual supergiants and H II regions (Sohn & Davidge 1996). Many previous studies focused on the H II regions; Belley & Roy (1992) derived reddenings, Hβ emission-equivalent widths and metallicities for 130 H II regions; Ivanov et al. (1992) classified a similar number of stellar associations. Sohn & Davidge (1996) studied a large number (more than 300) of stellar objects in the disc of NGC 628, measuring brightness and colours, finding some recent star formation and getting an estimate of the distance modulus (29.3 mag).

Our observations of NGC 628 are disturbed by the presence of a foreground star which falls close to the centre ($\approx$13 arcsec southern); as mentioned in the caption to Table 2 our first exposure on this galaxy was centred on this foreground star. During our last two exposures, the observing conditions were not optimal: the seeing went up to $\approx$2 arcsec.

From our data we can measure slow projected rotation around the minor axis, as expected for an almost face-on object. The stellar velocity dispersion decreases in the central zones, indicating a cold central region, maybe an inner disc. Photometric observations at UV wavelengths from Cornett et al. (1994) did not show evidence for a bulge: the nucleus of NGC 628 has the appearance of disc material in the UV. The ionized gas rotates in a way similar to the stars; the Hβ distribution turns out to be more extended than the [O III] distribution, both of them suggesting an annular structure.

6.4.3 NGC 772

NGC 772, named also Arp78, forms a pair at 3.3 arcmin with the E3 galaxy NGC 770. It is an Sb galaxy characterized by a particularly strong spiral arm; it is known to have faint H II regions (Oey & Kennicutt 1993) and extended H I, to a radius $\approx$75 kpc (Rao & Briggs 1993).

The unsharp-masked SAURON image (no optical *HST* image is available) displays a well-defined dust pattern, with the dust following the spiral arms. From the stellar kinematical maps, we can see that in the central region there is a clear drop in the stellar velocity dispersion and h_3 turns out to anticorrelate with the velocity, as expected for a rotating disc; the stellar velocity map shows rotation around the photometric minor axis and a mildly S-shaped zero-velocity line. The gas, especially in Hβ, rotates in a more complex way than the stars, with a very strongly S-shaped zero-velocity line, and its distribution follows the spiral arm pattern. The [O III] velocity field is instead much more regular. The gas velocity dispersion in the Hβ line is flat and low beyond $\approx$10 arcsec, enhanced in an annular region around the centre and depressed again in the nucleus –although still well higher than in the outer parts. All of this is also seen in the [O III]/Hβ map, where we can recognize regions with very low values corresponding to the spiral arms and to low values in the ionized-gas velocity dispersion.

6.4.4 NGC 864

Nuclear radio emission has been found in this barred Sc spiral galaxy (Ulvestad & Ho 2002); the nuclear radio source has diffuse morphology, with linear size of $\approx$300 pc.

The SAURON maps show rotation both in the stellar and gaseous components, around the photometric major axis, e.g. the rotation axis is oriented as the bar; but looking at a larger-scale image (see e.g. Fig. 2) we can see that the major axis of the bar turns out to be the global minor axis when considering the whole optical galaxy. The stellar velocity dispersion is flat and low over the entire SAURON FOV. The gas flux follows the nucleus plus bar structure, as visible especially in the Hβ case. The line ratio [O III]/Hβ is also structured in a similar way, assuming low values along the bar and in particular in the central $\approx$4-arcsec circle, which could indicate a star forming nucleus. Interestingly, this region corresponds to a local minimum in the Hβ velocity dispersion map, which assumes in the centre lower values than the dispersion in [O III], differently to what happens in most of our galaxies.

6.4.5 NGC 1042

This Scd galaxy forms a pair with the Sc galaxy NGC 1035 at a separation of 22 arcmin (corresponding to 177 kpc). It has a bright,

small nucleus and otherwise low surface brightness. Neutral hydrogen has been detected at positions corresponding to the optical centre and two adjacent regions (Bottinelli & Gouguenheim 1980).

In our data, this galaxy has a quite poor S/N, so that the stellar binning is quite heavy. There are some indications of slow projected stellar rotation, but in general the kinematical maps are difficult to interpret. The gas is quite patchy and does not cover, at the chosen A/N level, the whole SAURON field. In contrast to what is seen in the majority of our galaxies, the velocity dispersion in [O III] is higher than in Hβ, especially in the central region.

6.4.6 NGC 2805

NGC 2805 is an Sd galaxy seen nearly face-on and it is the brightest member of a multiple interacting system containing also NGC 2814 (Sb), NGC 2820 (Sc) at 13 arcmin and IC2458 (I0). According to Hodge (1975), in this group the H II regions appear distorted on the side of the galaxy opposite to the companion. H I has been detected (Reakes 1979; Bosma et al. 1980) and there are claims that the outer H I layers are warped (see e.g. Bosma et al. 1980). The galaxy seems to be also optically disturbed, since the spiral arms appear to be broken up into straight segments.

From our SAURON data, we find slow projected stellar velocities and a central drop in velocity dispersion. The gas has a clumpy distribution and rotates consistently with the stars. The line ratio [O III]/Hβ is low all over the field, possibly indicating ongoing star formation everywhere.

6.4.7 NGC 2964

NGC 2964 is a barred Sbc galaxy and forms a non-interacting pair with the I0 galaxy NGC 2968 at 5.8 arcmin. From *HST* images Carollo et al. (1997) detected a resolved central compact component, possibly star forming. CO has been detected by Braine et al. (1993); they suggested that the galaxy might contain an unresolved nuclear ring.

Our data reveal a variety of features in this galaxy. The stars rotate in a quite regular way, although a twist in the zero-velocity line can be seen very close to the edge of the field, on both sides. The stellar velocity dispersion increases smoothly towards the centre. Two-dimensional maps of stellar velocity and velocity dispersion for this galaxy have recently been published by Batcheldor et al. (2005). Although their maps deliver a lower spatial resolution than ours and a smaller FOV, there is a global agreement between the two observations. They also provide central values for the higher Gauss–Hermite moments h_3 and h_4; the latter value is larger than ours.

The ionized gas has a clumpy distribution, which could suggest a spiral arm structure, and complex kinematics in both lines, with a very irregular zero-velocity line and with the velocity dispersion peaking in an off-centre region. The velocity dispersion in [O III] is enhanced with respect to Hβ. Overall, the gas motions are consistent with the stellar rotation. In the region of the gas-σ peak, the spectra show also complex line profiles; in some bins we find double-peaked lines in the [O III] spectral region (see discussion in Section 4.2). It could be that we are seeing the regular gas motion together with an ionization cone, caused by a central active galactic nucleus (AGN), as is probably also the case in NGC 4102. Up to now, NGC 2964 has not been classified as an AGN yet. The double-peaked line shape characterizes only a few spectra, so we applied our standard method which fits single Gaussians to the emission lines. The [O III]/Hβ line ratio is small over most of the field, and is enhanced in a ring-like structure (see also Braine et al. 1993) surrounding an elongated nuclear region where the ratio becomes low again. This could be a star forming region, in accordance with Carollo et al. (1997).

6.4.8 NGC 3346

This is a barred Scd galaxy, for which only little information is available from the literature. The SAURON data show regular stellar rotation around an axis slightly misaligned with respect to the direction perpendicular to the bar, with complicated structures in the very inner regions; the stellar velocity dispersion is everywhere low and flat, and it seems to be depressed in a central region elongated in the same direction as the bar; the map is quite patchy. The ionized gas is concentrated along the bar and the spiral arms and rotates similarly to the stars, although the gas velocity fields appear quite patchy. The Hβ distribution is more extended than [O III]. The line ratio [O III]/Hβ is depressed along the bar, particularly in bubble-shaped spots, as the Hβ velocity dispersion does as well; these could be star forming regions.

6.4.9 NGC 3423

Also for this Scd galaxy there is not much literature to refer to. In the SAURON maps we measure slow projected stellar rotation and low velocity dispersion. The gas shows a clumpy distribution and rotates faster than the stars and around the same axis. [O III]/Hβ is everywhere low, possibly indicating wide-spread star formation.

6.4.10 NGC 3949

NGC 3949 is an Sbc galaxy in the Ursa Major cluster. Optical images show a diffuse extended halo (Tully et al. 1996). It has been observed with the Westerbork Synthesis Radio Telescope (Verheijen 1997): H I is detected well beyond the optical galaxy.

The SAURON maps show rotation both in the stellar and gaseous components. The stellar velocity dispersion indicates a cold inner region. This galaxy is part of the sample observed by Batcheldor et al. (2005); as in the case of NGC 2964, their reported central h_4 value is larger than ours. Integral-field observations of NGC 3949 are presented also by Westfall et al. (2005); their central values for the stellar velocity dispersion are in good agreement with ours; the agreement at larger radii and in the gas velocity dispersion is less satisfactory. The gas has a complex and clumpy distribution and its velocity fields present the same characteristics as the stellar one: global rotation and irregular zero-velocity line. The global appearance of the previously mentioned H I velocity field resembles our SAURON velocity maps. Overall, [O III]/Hβ is low, especially in a circumnuclear region. No correspondence between the line ratio and the highly complex gas velocity-dispersion maps is evident.

6.4.11 NGC 4030

Carollo et al. (1998) analysed the *HST* images of NGC 4030, and found tightly wound flocculent spiral structure reaching the nucleus and an irregular, exponential bulge. Our observations of NGC 4030 have a very high S/N, so that the data are of extremely good quality. The kinematical behaviour of this Sbc galaxy is characterized by very regular rotation of stars and gas around the minor axis. The velocity dispersion increases smoothly moving inwards, becoming possibly flat in the nuclear region (see Fig. 6), and the stellar h_3

anticorrelates with the velocity, as expected for a rotating disc. Our gas flux maps show a central concentration, although in Hβ some structure is visible that could be related to the spiral arms and/or dust lanes pattern: as can be seen in the unsharp-masked image and as already noticed by Carollo et al. (1998), the spiral arms and dust lanes structures extend down to the innermost scales. From long-slit Hα optical spectroscopy extended over $\approx$80 per cent of the optical image, Mathewson & Ford (1996) derive a rotation curve with maximum rotation velocity of $\approx$236 km s^{-1}. Our gas velocity regularly increases going outwards, up to a value of $\approx$180 km s^{-1} at the edges of the field. Since the outermost radius of our data is smaller than the one of the quoted observations, there is not necessarily a disagreement.

6.4.12 NGC 4102

NGC 4102 shows a bright central bar from which two tightly wound and dusty spiral arms depart (Verheijen 1997). In the NED data base, this object is classified as a LINER; it is known to be a powerful far-infrared galaxy (Young et al. 1989) and also to have a strong nuclear radio source (Condon et al. 1982). Devereux (1989) classified it as one of the most powerful nearby starburst galaxies. From optical spectroscopy of the ionized swept-up gas, Boer (1994) determined the time-scale of the central starburst wind to be of the order of 10^6 yr – a young starburst. Gonçalves, Véron-Cetty & Véron (1999) recognized a weak Seyfert2 component, mainly detected by the broadening of the [O III] lines. NGC 4102 has also been observed in CO: Jogee & Kenney (1996) found a compact CO morphology and a CO velocity field characterized in the inner 200 pc by purely circular motion, and a sharp discontinuity in gas kinematics at larger radii, around 3 arcsec; this could be due to streaming motions along the bar. H I has been detected in absorption against the bright central radio source (Verheijen 1997).

The signs of all the documented activity going on in this galaxy are detectable also in our SAURON maps: the gas kinematics turn out to be extremely complicated. As mentioned in the discussion in Section 6.3, this is the only case in our sample with a significant difference between the kinematics of the Hβ and [O III] lines: the Hβ velocity field resembles more closely the stellar one, although it is more irregular, while the [O III] maps trace more likely the outflowing gas. This can be also seen by looking at the gas flux maps: in [O III] the central gaseous concentration appears to be elongated in a north-western direction, which is not the case in the Hβ distribution, that follows instead the spiral arm pattern. The [O III] velocity dispersion is also elongated in the same direction. Together with NGC 2964, this is the only galaxy in our sample where we find emission lines that are not well fitted by single Gaussians (see the discussion in Section 4.2 and Fig. 3). The complex line profiles are found only in the region corresponding to the maximum difference between the Hβ and [O III] kinematics (which is also, as already noticed, the region of the [O III] σ peak and flux elongation); there the [O III] lines turn out to be broadened, in accordance with Gonçalves et al. (1999). According to our measurements, the [O III]/Hβ line ratio is then enhanced in the outflow region, as expected for an active object. As for the stellar kinematics, we do not see signs of activity there: the stars behave in a much more quiet way, with regular rotation and velocity dispersion increasing from the outer parts towards the centre.

6.4.13 NGC 4254

NGC 4254, known also as M99, is one of the brightest spiral galaxies in the Virgo cluster. Its optical appearance is characterized by the one-arm structure: the arms to the north-west are much less defined than the southern arm. This kind of spiral structure could be related to an external driving mechanism, but for NGC 4254 there are no close companions and no evident signs of past interactions (Rauscher 1995). Phookun, Vogel & Mundy (1993) carried out H I and Hα observations of this Sc galaxy, detecting non-disc H I emission, coming mostly from a region to the north of the galaxy and contiguous with it in the plane of the sky; according to the authors, the non-disc H I corresponds to 3 per cent of the total H I mass; they do not find Hα emission corresponding to the non-disc gas, which indicates little or no star formation there. They interpreted these observational results as infall of a disintegrating gas cloud; this could have caused the asymmetry in the spiral structure. Hα intensity and velocity fields are presented also in Chemin et al. (2006), confirming the asymmetry in the prominent spiral structure and detecting streaming motions along the arms. There are also claims for the presence of a weak bar with a PA of $\approx$60°, although NGC 4254 is classified as unbarred (Sakamoto et al. 1999, from analysis of the molecular gas distribution).

We observed this galaxy under bad seeing conditions ($\approx$3 arcsec). Our kinematic maps reveal regular stellar rotation, although the stellar zero-velocity line is twisting towards the edges of the field. The gas flux follows the spiral pattern, which is particularly evident in the Hβ case and can be seen also in the [O III]/Hβ line ratio, which assumes particularly low values in bubble-shaped regions along the arms. The gas rotation globally resembles the stellar motions, but presents more complex structures, with S-shaped zero-velocity lines, which could be related to the mentioned possible bar; Fourier analysis of the velocity field will help clarifying this. Velocity dispersion in [O III] is higher than in Hβ, as particularly visible in the central region.

6.4.14 NGC 4487

This Scd galaxy forms a pair with the Scd galaxy NGC 4504, at a separation of 35 arcmin (corresponding to $\approx$165 kpc). Two principal arms of the grand-design type are recognizable in the images; one of the two is less well defined than the other and splits into broad segments which cover one side of the disc. The spiral pattern shows up also in our gas flux maps. The stars and gas rotate around an axis misaligned with respect to the photometric minor axis. The stellar and gaseous velocity dispersions are everywhere very low. In the [O III]/Hβ map regions of possible star formation can be recognized, in the centre and along the spiral arm, in correspondence to a drop in the Hβ velocity dispersion. Contrary to what happens in the majority of our galaxies, in the very centre the velocity dispersion in Hβ is lower than that in [O III].

6.4.15 NGC 4775

Very little is known about this low-inclination and very late-type (Sd) galaxy. Our maps, although based on 4 $\times$ 1800-s exposures, are quite patchy and not easy to interpret; they suggest very slow stellar and gaseous projected rotation, as expected for an almost face-on galaxy, low stellar and gaseous velocity dispersion and a clumpy gas distribution in both Hβ and [O III] lines.

6.4.16 NGC 5585

NGC 5585 is a barred Sd galaxy; together with NGC 5204 (Sm), NGC 5474 (Scd), NGC 5477 (Sm), HoIV (Im) and M101 (Scd) it

forms the M101 group. It is highly resolved into individual stars and H II regions. In this galaxy, Coté, Carignan & Sancisi (1991) detected H I extended out to more than twice the optical radius; the H I velocity field turned out to be strongly warped; using these data and the *B*-band luminosity profiles, they constructed a mass model finding that the contribution of the dark matter component dominates the rotation curve at almost all radii, also when using a maximum-disc method. Later, Blais-Ouellette et al. (1999) pointed out that using two-dimensional Hα Fabry–Pérot spectroscopy one can better constrain the orientation parameters and the rotation curve in its rising part, reducing by 30 per cent the dark to luminous matter ratio.

In our SAURON maps, there is not much information about the stellar velocity (patchy map). There are some hints of slow projected rotation. The stellar σ decreases moving outwards from the central region, although the map appears patchy and has everywhere low values. The gas distribution follows the bar morphology; along the bar some spots can be seen where the flux in [O III] is larger than that in Hβ. The [O III]/Hβ line ratio is enhanced in a region elongated in a roughly perpendicular direction to the one defined by the bar.

6.4.17 NGC 5668

NGC 5668 is another Sd galaxy, which has a high rate of star formation, as indicated by its large far-infrared and Hα luminosities (Schulman et al. 1996, and references therein); the mentioned authors observed it in H I and detected high-velocity clouds of neutral hydrogen. High-velocity clouds were found also in the ionized gas and interpreted as regions with vertical motions related to ongoing star forming processes in the disc, as pointed out by Jiménez-Vicente & Battaner (2000) on the basis of Fabry–Pérot Hα observations.

Our SAURON data indicate very slow stellar projected rotation velocities and a cold inner region. The gas distribution is clumpy, defining a ring-like structure also characterized by slightly lower [O III]/Hβ values compared to the surroundings.

6.4.18 NGC 5678

Not much is known from previous work on this barred and very dusty Sb galaxy. According to our SAURON data, the stars rotate in a rather regular way around the minor axis, although the zero-velocity line is strongly bent. The stellar velocity dispersion increases moving inwards, and becomes flatter in the nuclear region (see Fig. 6). The gas has instead a complex distribution, more structured in Hβ than in [O III], with kinematics consistent with the stars, but a zero-velocity line more disturbed and wiggling, similar to what we see in NGC 2964. Over a large part of the field, the velocity dispersion in the [O III] line is higher than in Hβ.

7 CONCLUSIONS

Two-dimensional kinematics and stellar population analysis of spiral galaxies towards the end of the Hubble sequence (Hubble types later than Sb) is still a relatively unexplored field: late-type spirals are very complex objects, often faint and full of substructures, as recently proved by analysis of *HST* images. They have been the targets of a few photometric and long-slit optical spectroscopic observations, but measurements of their two-dimensional kinematics were still missing. We have started a project on a sample of 18 such objects using integral-field spectroscopic observations obtained with SAURON. This allowed us to measure the stellar kinematics, the flux and kinematics of the Hβ 4861 Å and [O III]$\lambda\lambda$4959, 5007 Å emission lines and the strength of the Hβ, Fe and Mg*b* absorption features over a two-dimensional area covering the central region of our galaxies.

In this paper, we discussed the first results from this study, presenting the two-dimensional kinematics for stars and ionized gas. The majority of our galaxies is shown to be kinematically cold and to possess a considerable amount of ionized gas, covering in most cases a large part of the SAURON FOV and frequently following bar or spiral arm patterns in the spatial distribution. A quite common feature of our measured stellar kinematical maps is a central depression in the velocity dispersion, which assumes very often low values; we measured the velocity dispersion profiles and correlated their slopes with the morphological type: later-type galaxies tend to have velocity dispersion profiles which increase outwards. This implies small bulge/disc ratios and the presence of inner, occasionally star forming, disc-like structures. We also qualitatively compared the characteristics of our maps with the properties of the galaxy known from literature *HST* isophotal analysis: the main conclusion common to spectroscopy and photometry is that the kinematic detection of a cold inner region turns out to be often related to the lack of a classical stellar bulge and the presence of small-scale structures (nuclear star clusters, inner rings, inner bars). The gaseous component turns out to be almost ubiquitous and kinematically highly complex, displaying in many cases irregular velocity fields, with the kinematic axis twisting or bending or wiggling, or even without a clear sense of rotation, possibly because of the dust which strongly affects these objects. They also host intense star formation, often spread over the whole region we have observed, as suggested by the low values in the [O III]/Hβ line ratio maps.

In follow-up papers we will model the observed kinematic fields in detail, present the line-strength maps for these same galaxies, consider the bulge–disc decomposition and compare our results with those for the 24 Sa bulges in the SAURON survey.

ACKNOWLEDGMENTS

We kindly acknowledge Anna Pasquali and Ignacio Ferreras for their help during the early stages of this project. We thank Marc Balcells, Marc Sarzi and Kristen Shapiro for a careful reading of and commenting on the draft. We also thank the referee Torsten Böker for useful comments and suggestions which improved the paper. The SAURON-related projects are made possible through grants 614.13.003, 781.74.203, 614.000.301 and 614.031.015 from NWO and financial contributions from the Institut National des Sciences de l'Univers, the Université Claude Bernard Lyon I, the Universities of Durham, Leiden and the Netherlands Research School for Astronomy NOVA. KG acknowledges support for the Ubbo Emmius PhD program of the University of Groningen. JFB acknowledges support from the Euro3D Research Training Network, funded by the EC under contract HPRN-CT-2002-00305. MC acknowledges support from a VENI grant 639.041.203 awarded by the Netherlands Organization for Scientific Research (NWO). This project made use of the HyperLeda and NED data bases. Part of this work is based on data obtained from the STSci Science Archive Facility. The Digitized Sky Surveys were produced at the Space Telescope Science Institute under US Government grant NAGW-2166. The images of these surveys are based on photographic data obtained using the Oschin Schmidt Telescope on Palomar Mountain and the UK Schmidt Telescope.

REFERENCES

Allard E. L., Peletier R. F., Knapen J. H., 2005, ApJ, 633, L25
Andredakis Y., Sanders R., 1994, MNRAS, 267, 283
Andredakis Y. C., Peletier R. F., Balcells M., 1995, MNRAS, 275, 874
Bacon R. et al., 2001, MNRAS, 326, 23 (Paper I)
Batcheldor D. et al., 2005, ApJS, 160, 76
Belley J., Roy J.-R., 1992, ApJS, 78, 61
Blais-Ouellette S., Carignan C., Amram P., Coté C., 1999, AJ, 118, 2123
Boer B., 1994, in Shlosman I., ed., Mass Transfer Induced Activity in Galaxies. Cambridge Univ. Press, Cambridge, p. 308
Böker T., Laine S., van der Marel R. P., Sarzi M., Rix H.-W., Ho L. C., Shields J. C., 2001, A&AS, 199, 705
Böker T., Laine S., van der Marel R. P., Sarzi M., Rix H.-W., Ho L. C., Shields J. C., 2002, AJ, 123, 1389
Böker T., van der Marel R. P., Gerssen J., Walcher J., Rix H.-W., Shields J. C., Ho L. C., 2003, SPIE, 4384, 57
Bosma A., Casini C., Heidmann H., van der Hulst J. M., van Woerden H., 1980, A&A, 89, 345
Bottinelli L., Gouguenheim L., 1980, A&A, 88, 108
Braine J., Combes F., Casoli F., Dupraz C., Gerin M., Klein U., Wielebinski R., Brouillet N., 1993, A&AS, 97, 887
Briggs F. H., Wolfe A. M., Krumm N., Salpeter E. E., 1980, ApJ, 238, 510
Briggs F. H., 1982, ApJ, 259, 544
Cappellari M., Copin Y., 2003, MNRAS, 342, 345
Cappellari M., Emsellem E., 2004, PASP, 116, 138
Carollo C. M., 1999, ApJ, 523, 566
Carollo C. M., Stiavelli M., 1998, AJ, 115, 2306
Carollo C. M., Stiavelli M., de Zeeuw P. T., Mack J., 1997, AJ, 114, 2366
Carollo C. M., Stiavelli M., Mack J., 1998, AJ, 116, 68
Carollo C. M., Stiavelli M., Seigar M., de Zeeuw P. T., Dejonghe H., 2002, AJ, 123, 159
Chen P. C. et al., 1992, ApJ, 395, 41
Chemin L. et al., 2006, MNRAS, in press (astro-ph/0511417)
Combes F., Debbasch F., Friedli D., Pfenniger D., 1990, A&A, 233, 82
Condon J. J., Condon M. A., Grisler G., Puscell J. J., 1982, ApJ, 252, 102
Cornett R. H. et al., 1994, ApJ, 426, 553
Coté S., Carignan C., Sancisi R., 1991, AJ, 102, 904
Courteau S., de Jong R., Broeils A. H., 1996, ApJ, 457, 73
de Jong R., 1995, PhD thesis, Univ. Groningen, the Netherlands
de Jong R., 1996, A&A, 313, 45
de Vaucouleurs G., de Vaucouleurs A., Corwin H. G. Jr., Buta R. J., Paturel G., Fouqué P., 1991, Third Reference Catalogue of Bright Galaxies. Springer-Verlag, New York (RC3)
de Zeeuw P. T. et al., 2002, MNRAS, 329, 513 (Paper II)
Devereux N. A., 1989, ApJ, 346, 126
D'Onofrio M., Zaggia S. R., Longo G., Caon N., Capaccioli M., 1995, A&A, 296, 319
Emsellem E., Greusard D., Combes F., Friedli D., Leon S., Pécontal E., Wozniak H., 2001, A&A, 368, 52
Emsellem E. et al., 2004, MNRAS, 352, 721 (Paper III)
Falcón-Barroso J., Peletier R. F., Balcells M., 2002, MNRAS, 335, 741
Falcón-Barroso J. et al., 2006, MNRAS, submitted (Paper VII)
Fall S. M., Efstathiou G., 1980, MNRAS, 193, 189
Fuchs B., 1997, A&A, 328, 43
Gerhard O. E., 1993, MNRAS, 265, 213
Gerssen J., Kuijken K., Merrifield M. R., 1997, MNRAS, 288, 618
Gonçalves A. C., Véron-Cetty M.-P., Véron P., 1999, A&AS, 135, 437
Grosbøl P. J., 1985, A&AS, 60, 261
Ho L. C., Filippenko A. V., Sargent W. L., 1995, ApJS, 98, 477
Ho L. C., Filippenko A. V., Sargent W. L., 1997, ApJS, 112, 315
Hodge P. W., 1975, ApJ, 202, 619
Ivanov G. R., Popravko G., Efremov I. N., Tikhonov N. A., Karachentsev I. D., 1992, A&AS, 96, 645
James P. A., Seigar M. S., 1999, A&A, 350, 791
Jiménez-Vicente J., Battaner E., 2000, A&A, 358, 812
Jogee S., Kenney J. D. P., 1996, ASPC, 91, 230
Jones L., 1997, PhD thesis, Univ. North Carolina
Kennicutt R. C. et al., 2003, PASP, 115, 928
Kormendy J., 1984, ApJ, 286, 132
Laine S., Shlosman I., Knapen J. H., Peletier R. F., 2002, ApJ, 567, 92
MacArthur L., Courteau S., Holtzmann J., 2003, ApJ, 582, 689
Márquez I., Masegosa J., Durret F., González Delgado R. M., Moles M., Maza J., Pérez E., Roth M., 2003, A&A, 409, 459
Matthews L. D., Gallagher J. S., 2002, ApJS, 141, 492
Mathewson D. S., Ford V. L., 1996, ApJS, 107, 97
Natali G., Pedichini F., Righini M., 1992, A&A, 256, 79
Norman C., Sellwood J. A., Hasan H., 1996, ApJ, 462, 114
Oey M. S., Kennicutt R. C., 1993, ApJ, 411, 137
Peletier R. F., Knapen J. H., Shlosman I., Pérez-Ramírez D., Nadeau D., Doyon R., Rodriguez Espinosa J. M., Pérez García A. M., 1999, ApJS, 125, 363
Pérez-Ramírez D., Knapen J. H., Peletier R. F., Laine S., Doyon R., Nadeau D., 2000, MNRAS, 317, 234
Peterson C. J., 1980, AJ, 85, 226
Pfenniger D., Norman C., 1990, ApJ, 363, 391
Phookun B., Vogel S. N., Mundy L. G., 1993, ApJ, 418, 113
Raha N., Sellwood J. A., James R. A., Kahn F. D., 1991, Nature, 352, 411
Rao S., Briggs F., 1993, ApJ, 419, 515
Rauscher B. J., 1995, AJ, 109, 1608
Reakes M., 1979, MNRAS, 187, 525
Roberts M. S., 1962, AJ, 67, 437
Sakamoto K., Okumura S. K., Ishizuk S., Scoville N. Z., 1999, ApJS, 124, 403
Sarzi M. et al., 2006, MNRAS, in press (doi:10.1111/j.1365-2966.2005.09839.x) (astro-ph/0511307) (Paper V)
Schulman E., Bregman J. N., Brinks E., Roberts M. S., 1996, AJ, 112, 960
Seigar M. S., 2002, A&A, 393, 499
Seigar M. S., Carollo C. M., Stiavelli M., de Zeeuw P. T., Dejonghe H., 2002, AJ, 123, 184
Shapiro K. L., Gerssen J., van der Marel R. P., 2003, AJ, 126, 2707
Silk J., 2003, Astrophys. Space Sci., 284, 663
Sohn Y.-J., Davidge T. J., 1996, AJ, 111, 2280
Tonry J., Davis M., 1981, ApJ, 246, 666
Tully R. B., Verheijen M. A. W., Pierce M. J., Huang J.-S., Wainscoat R. J., 1996, AJ, 112
Ulvestad J. S., Ho L. C., 2002, ApJ, 581, 925
van der Marel R. P., Franx M., 1993, ApJ, 407, 525
Vazdekis A., 1999, ApJ, 513, 224
Verheijen M., 1997, PhD thesis, Univ. Groningen, the Netherlands
Verheijen M., 2001, ApJ, 563, 694
Wakker B. P., Adler D. S., 1995, AJ, 109, 134
Walcher C. J. et al., 2005, ApJ, 618, 237
Westfall K. B., Bershady M. A., Verheijen M. A. W., Andersen D. R., Swaters R. A., 2005, preprint (astro-ph/0508552)
Whitmore B. C., Kirshner R. P., Schechter P. L., 1979, ApJ, 234, 68
Wozniak H., Combes F., Emsellem E., Friedli E., 2003, A&A, 409, 469
Wyse R. F. G., Gilmore G., Franx M., 1997, ARA&A, 35, 637
Yahil A., Tammann G. A., Sandage A., 1977, ApJ, 217, 903
Young J. S., Xie S., Kenney J. D. P., Rice W. L., 1989, ApJS, 70, 699

This paper has been typeset from a TEX/LATEX file prepared by the author.